

Error-Mitigated Quantum Metrology via Probabilistic Virtual Purification

Xiaodie Lin^{1,4} and Haidong Yuan^{1,2,3*}

¹*Department of Mechanical and Automation Engineering,*

The Chinese University of Hong Kong, Hong Kong SAR, China

²*The Hong Kong Institute of Quantum Information Science and Technology,*

The Chinese University of Hong Kong, Shatin, Hong Kong SAR, China

³*State Key Laboratory of Quantum Information Technologies and Materials,*

The Chinese University of Hong Kong, Shatin, Hong Kong SAR, China

⁴*College of Computer and Data Science, Fuzhou University, Fuzhou 350116, China*

Quantum metrology stands as a leading application of quantum science and technology, yet its precision and sensitivity are often constrained by noise. In the context of near-term quantum metrology, quantum error mitigation offers a promising strategy to leverage quantum resources. While existing error-mitigated protocols largely depend on virtual state purification, significant noise accumulation and the additional noise introduced by the noisy implementations of these protocols can impede the effectiveness. To address these problems, we propose probabilistic virtual channel purification to handle the largely accumulated noise while efficiently canceling additional noise from itself. This also naturally leads to an enhanced version of virtual state purification, namely probabilistic virtual state purification. Within the sequential scheme of quantum metrology, our error analysis reveals a significant reduction in bias and a quantum advantage in sampling cost when the number of channels encoding the interested parameters is $O(p^{-1})$, where p is the error rate of the encoding channel. In this range, both probabilistic virtual purification methods demonstrate significant improvements in parameter estimation precision and robustness against practical noise, as evidenced by numerical simulations for both single- and multi-parameter tasks.

I. INTRODUCTION

Quantum metrology is one of the most promising applications of quantum science and technology [1–4]. Quantum resources, such as coherence and entanglement, can be employed to enhance the sensitivity to reach the Heisenberg limit. However, due to the existence of decoherence or other sources of noise, the achievable precision and sensitivity of quantum metrology could be limited [5–7].

Quantum error correction (QEC) is a promising approach to address noise limitations in quantum metrology, with numerous studies demonstrating its potential to enhance measurement precision [8–13]. However, practical implementation of QEC faces significant challenges, including noise in ancillary qubits, imperfect error correction operations, and often unrealistic theoretical assumptions. Though much progress has been made recently [14–16], the current stage of quantum technology is still in the early phase of the noisy intermediate-scale quantum (NISQ) era, which takes a long transition towards fully fault-tolerant quantum computing [17]. In the NISQ era, quantum error mitigation (QEM) has emerged as a practical alternative that can extract useful quantum advantage from imperfect devices [18–22]. Unlike QEC, which aims to correct errors in individual quantum circuits, QEM reduces the noise-induced bias in the expectation value by post-processing outputs from an ensemble of noisy circuits. This approach significantly relaxes the experimental precision requirements compared

to full QEC, making it particularly suitable for near-term quantum devices [23–26].

Since virtual state purification (VSP) [22, 27] does not require characterization of noise models, existing error-mitigated quantum metrology protocols are based primarily on it [23–25]. The basic idea of VSP is to exponentially suppress errors using collective measurements of m copies of the target quantum state ρ to measure the values with respect to the state $\rho^m/\text{tr}(\rho^m)$. However, this approach imposes stringent requirements: (i) both input and ideal output states must remain pure throughout the protocol, and (ii) the noiseless component must dominate the noisy output state. These conditions become particularly challenging in quantum metrology applications, where repeated channel use for parameter encoding leads to large system sizes or deep quantum circuits. Consequently, error accumulation causes significant misalignment between the dominant noisy component and the ideal output state, leading to the failure of VSP.

To address these limitations, we first introduce virtual channel purification (VCP) [28] to quantum metrology. This approach offers distinct advantages over VSP by allowing error mitigation at arbitrary circuit locations rather than solely at the final output state. Therefore, errors in quantum metrology can be suppressed before they are too large to mitigate. However, both VSP and VCP rely on performing collective quantum operations on different quantum subsystems to “purify” the target quantum state. These operations may introduce substantial noise to physical experiments, thereby limiting the practical effectiveness of these methods.

To further address this problem, we propose probabilistic virtual channel purification (PVCP) that incorporates

* Email: hdyuan@mae.cuhk.edu.hk

probabilistic error cancellation (PEC) [19, 20] specifically tailored to VCP. Here, we focus on the sequential feed-back scheme of quantum metrology, as it has been shown to outperform the parallel scheme in Hamiltonian parameter estimation and is more experiment-friendly [29]. Concretely, our analysis of the impact of noise at various positions within VCP circuits reveals the existence of noise at certain positions that introduces no systematic errors. Consequently, PEC is strategically applied only at critical positions to efficiently cancel errors. The strategy for applying PEC can be naturally adapted for VSP, leading to the probabilistic virtual state purification (PVSP).

Notice that the cost of exactly mitigating general noise grows exponentially with the number of noisy quantum operations [30–32], which can easily overwhelm the polynomially enhanced precision in quantum metrology [33–36]. Notably, the error analysis of PVCP indicates the significant reduction of bias while maintaining quantum advantage when the number N of utilized encoding channels, each with an error rate p , is no more than the order of p^{-1} . For N in the range of $O(p^{-1})$, the effectiveness of both probabilistic virtual purification methods is systematically demonstrated through numerical simulations for both single- and multi-parameter estimation tasks. Our results not only exhibit a significant improvement in the precision of the estimated parameters but also showcase their robustness against practical noise and imperfect noise model characterization.

II. SETTINGS AND TYPICAL QUANTUM ERROR MITIGATION METHODS

In a typical quantum metrology setup, a probe state ρ is prepared then evolved into ρ_{λ} through one or more applications of an encoding unitary U_{λ} , which contains K unknown parameters $\lambda = (\lambda_1, \lambda_2, \dots, \lambda_K)$. Information about λ can be extracted using a positive operator-valued measurement (POVM) $\{E_x\}$, where $\sum_x E_x = I$. The probability of obtaining a specific measurement outcome x is determined by the Born rule $P(x|\lambda) = \text{tr}(E_x \rho_{\lambda})$. By repeating this measurement process many times, a sequence of outcomes is collected. From this data, an estimate $\hat{\lambda} = (\hat{\lambda}_1, \hat{\lambda}_2, \dots, \hat{\lambda}_K)$ of the unknown parameters λ can be derived. Fig. 1 illustrates the sequential feedback scheme for this process regarding the multiple uses of U_{λ} . The green boxes represent quantum gates, while the red circles indicate local noise occurring immediately after each quantum gate due to imperfect quantum operations. We visualize the state and measurement preparation processes with noise in the two gray boxes, respectively, and the output state is subsequently measured on a computational basis. The blue box represents the parameter encoding stage. In this scheme, immediate feedback control, denoted as V_i , is allowed after each application of the encoding unitary U_{λ} .

To suppress the effects of noise in quantum metrology,

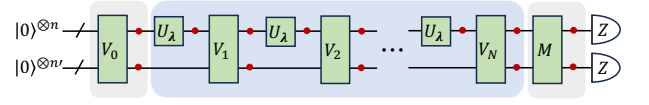


FIG. 1: Sequential feedback scheme of quantum metrology. Green boxes represent quantum gates, while red circles indicate local noise occurring immediately after each quantum gate. Particularly, the first gray box, the blue box and the final gray box represent the state preparation stage, parameter encoding stage and measurement preparation stage, respectively. Subsequently, the output state is measured on a computational basis.

VSP-based quantum metrology has been proposed to enhance the precision and sensitivity of parameter estimation [23–25]. Specifically, m copies of the target state ρ are utilized to measure expectation values with respect to the state

$$\bar{\rho}^m := \frac{\rho^m}{\text{tr}(\rho^m)} = \frac{\sum_i p_i^m |i\rangle \langle i|}{\sum_i p_i^m},$$

where $\rho = \sum_i p_i |i\rangle \langle i|$ represents the spectral decomposition of ρ . This approach exponentially suppresses the relative weights of the nondominant eigenvectors in m . Fig. 2(a) exemplifies the circuit implementation of VSP when $m = 2$, where the error-mitigated expectation value of the observable O is given by

$$\frac{\langle X \otimes O \rangle}{\langle X \otimes I_{2^n} \rangle} = \frac{\text{tr}(O \bar{\rho}^2)}{\text{tr}(\bar{\rho}^2)},$$

with the sampling cost $C_{\text{em}} \sim \text{tr}(\bar{\rho}^2)^{-2}$ [22]. However, it is important to note that VSP can only be applied to the output state. If the circuit is too complex and accumulates significant errors, causing the dominant eigenvector of $\bar{\rho}^m$ to deviate substantially from the noise-free state, VSP-based quantum metrology might not ensure even a constant factor reduction in the bias [24].

To tackle this problem, we now introduce VCP to quantum metrology [28]. In practice, suppose a quantum unitary channel \mathcal{U} is followed by the noise channel $\mathcal{E} = p_0 \mathcal{I}_{2^n} + \sum_{i=1}^{4^n-1} p_i \overline{E_i}$, where \mathcal{I}_{2^n} stands for the 2^n -dimensional identity channel and $\overline{E_i}(\rho) = E_i \rho E_i^\dagger$ denotes the channel for a given error component. Crucially, we require $p_0 > p_i$ for all i , meaning the leading component of \mathcal{E} is the identity channel. Consistent with the assumptions made in VSP [22, 27], the noise channel \mathcal{E} is assumed to be Pauli noise, with E_i being Pauli operations. For general noise, it can be converted into Pauli noise using Pauli twirling [37, 38]. Define $\mathcal{U}_{\mathcal{E}} = \mathcal{E} \circ \mathcal{U}$. The goal of VCP is to exploit m copies of $\mathcal{U}_{\mathcal{E}}$ to realize $\mathcal{U}_{\mathcal{E}^{(m)}} = \mathcal{E}^{(m)} \circ \mathcal{U}$, where the purified noise channel is of

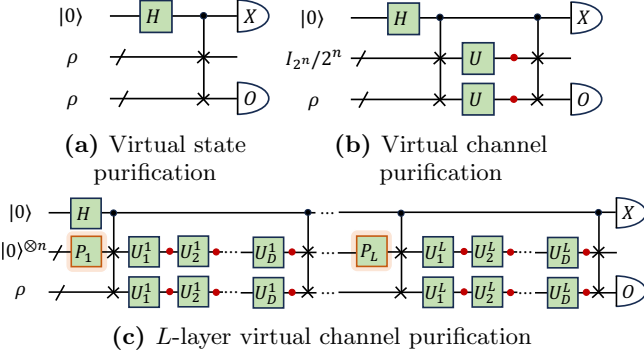


FIG. 2: Circuit implementation of (a) VSP, (b) VCP and (c) L -layer VCP with $m = 2$. The red circles represent noise in the target quantum circuit, while the implementation of VSP and VCP is assumed to be noise-free here. Quantum gates P_i in the orange boxes are the tensor product of single-qubit random Pauli unitaries.

the form

$$\mathcal{E}^{(m)} = \frac{1}{\sum_{i=0}^{4^n-1} p_i^m} \left(p_0^m \mathcal{I}_{2^n} + \sum_{i=1}^{4^n-1} p_i^m \mathbf{E}_i \right).$$

Since the identity channel \mathcal{I}_{2^n} is the dominant component, the noise rate of $\mathcal{E}^{(m)}$ decreases exponentially as m increases. The circuit implementation of VCP with $m = 2$ is illustrated in Fig. 2(b). Similarly, the error-mitigated expectation value of the observable O is given by

$$\frac{\langle X \otimes O \rangle}{\langle X \otimes \mathcal{I}_{2^n} \rangle} = \text{tr} \left(O \mathcal{E}^{(2)} \circ \mathcal{U}(\rho) \right).$$

Let $P_m = \sum_{i=0}^{4^n-1} p_i^m$, the sampling cost is $C_{\text{em}} \sim P_m^{-2}$, which is similar to that obtained for VSP. However, compared with VSP, VCP can provide even exponentially stronger error suppression for global noise, as discussed in Ref. [28].

For a sequence of quantum operations, instead of applying VCP to the entire circuit, we can adopt a layer-wise implementation of VCP, as illustrated in Fig. 2(c). This approach allows for error suppression before it accumulates as the dominant component of the noise channel, thereby circumventing the issues encountered in VSP. Specifically, the control qubit can be reused for each layer. Instead of resetting the ancillary input to the maximally mixed state, random unitary gates can be utilized to achieve the same effect. Notably, since the Pauli group forms a unitary 1-design, we can simply apply random Pauli gates between two layers of VCP to replace the maximally mixed state, as depicted by the orange boxes in Fig. 2(c). Moreover, this method of implementing the maximally mixed state does not increase the sample complexity of VCP [28].

III. PROBABILISTIC VIRTUAL PURIFICATION

Since VCP can mitigate noise before it gets out of control and has stronger error suppression capability compared to VSP, we introduce it to improve the precision of quantum metrology. However, though VCP is theoretically effective, its practical performance is hindered by noise that occurs during the execution of these protocols. In particular, the controlled-SWAP (cSWAP) gate is notably noisy due to its complex implementation [39]. In Appendix A, we examine the performance of these virtual purification methods with and without cSWAP noise in a single-parameter estimation task. The results show that VCP achieves higher precision than VSP, but the benefits of both VCP and VSP are diminished, or can even be negated, in certain scenarios due to this noise. Thus, additional QEM methods should be considered to address the noise in cSWAP gates.

To exactly mitigate errors, PEC is adopted to enhance the performance of these virtual purification methods. The sampling cost and the number of different quantum circuits involved in PEC can grow exponentially with the number of noise locations (please refer to Appendix B for more details on PEC). In fact, for general noise this exponential growth is theoretically unavoidable for mitigating general noise exactly [30–32]. For a n -qubit quantum state ρ , the m th-order VCP introduces noise at $O(mn)$ locations. Although in the sequential scheme of quantum metrology $n = O(1)$ usually holds, given limited experimental resources in practice, a natural question arises: Can we reduce the sampling cost and the number of different circuits needed further for the VCP circuit rather than trivially applying PEC to all noise locations? The answer, as it turns out, is yes.

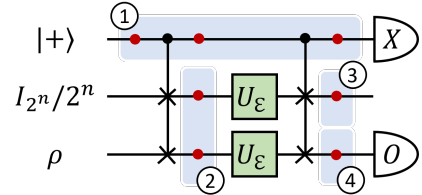


FIG. 3: Four categories of noise in the VCP circuit.

Take the single-layer VCP circuit with $m = 2$ for example, and the insights gained can be naturally extended to larger m . The input quantum state in the VCP circuit reads $|+\rangle\langle+| \otimes I_{2^n}/2^n \otimes \rho \in \mathcal{H}_{\text{ctrl}}^2 \otimes \mathcal{H}_{\text{anc}}^{2^n} \otimes \mathcal{H}_{\text{tar}}^{2^n}$, where $\mathcal{H}_{\text{ctrl}}$, $\mathcal{H}_{\text{anc}}^{2^n}$ and $\mathcal{H}_{\text{tar}}^{2^n}$ refer to the Hilbert spaces of the control (first), ancillary (second) and target (last) subsystems shown in Fig. 2 (b), respectively. Assuming local noise models, the noise introduced by the VCP circuit can be divided into four categories: ① noise in the control subsystem, ② noise in the last two subsystems between two cSWAP layers and ③ (④) noise in the ancillary (target) subsystem after the second cSWAP layer,

as illustrated in Fig. 3. For noise in ②, it is naturally mitigated by the VCP method, and noise in ③ can be ignored since it has no impact on the final result. Additionally, the noise in ④ only affects the measurement results of the observable O . Therefore, its impact on the final result varies depending on the observable O , while for an arbitrary observable O , additional QEM protocols can be introduced to realize the full benefits of VCP.

Noise in ① is the most complex case. Suppose each noise in ① is characterized by the quantum channel \mathcal{F} , and the noise between the cSWAP layers in each of the ancillary and target subsystems is represented by the quantum channel \mathcal{E} . Then, according to the following theorem, it turns out that many types of errors in the control subsystem do not introduce systematic error; rather, they only increase statistical error.

Theorem 1 Suppose noise channels $\mathcal{E} = \sum_{i=0}^{4^n-1} p_i \overline{E_i}$ and $\mathcal{F} = \sum_{i=0}^3 q_i \overline{F_i}$ are completely positive trace-preserving (CPTP) channels satisfy the properties

$$\text{tr}(E_i E_j^\dagger)/2^n = \begin{cases} 0, & i \neq j \\ e_i, & i = j \end{cases}$$

and

$$\mathcal{F}(|i\rangle\langle j|) = \begin{cases} f_{ij}|i\rangle\langle j|, & i \neq j \\ \sum_k f_k^{(i)}|k\rangle\langle k|, & i = j \end{cases}$$

where $e_i \in \mathbb{R}$ and $f_{ij}, f_k^{(i)} \in \mathbb{C}$. Then, for a local noise channel \mathcal{F} and an n -qubit quantum state ρ , it holds that

$$\frac{\langle X \otimes O \rangle_{\tilde{\rho}_{\text{out}}}}{\langle X \otimes I_{2^n} \rangle_{\tilde{\rho}_{\text{out}}}} = \frac{\langle X \otimes O \rangle_{\rho_{\text{out}}}}{\langle X \otimes I_{2^n} \rangle_{\rho_{\text{out}}}},$$

where $\tilde{\rho}_{\text{out}}$ and ρ_{out} denote the output states of the virtual channel purification circuit, with and without the existence of \mathcal{F} , respectively.

By directly calculating the expectation values, it holds that $\langle X \otimes O \rangle_{\tilde{\rho}_{\text{out}}} = \eta_m \text{tr} \left(O \hat{\mathcal{E}}^{(m)}(\rho) \right)$ and $\langle X \otimes I_{2^n} \rangle_{\tilde{\rho}_{\text{out}}} = \eta_m$, where $\hat{\mathcal{E}}^{(m)} = \hat{P}_m^{-1} \left(p_0^m e_0^{m-1} \mathcal{I} + \sum_{i=1}^{4^n-1} p_i^m e_i^{m-1} \overline{E_i} \right)$ with $\hat{P}_m = \sum_{i=0}^{4^n-1} p_i^m e_i^{m-1}$, and $\eta_m := \text{Real}(f_{01}^3) \hat{P}_m$. Meanwhile, in the absence of \mathcal{F} , the expectation values are similar but with $\text{Real}(f_{01}^3) = 1$. Therefore, by dividing these two expectation values, the effect of \mathcal{F} is canceled, resulting in the same result as if \mathcal{F} were not present. Please refer to Appendix C1 for more details.

Based on the properties discussed in Theorem 1, we can identify specific types of noise channels that satisfy these conditions. For example, \mathcal{E} can be noise channels such as the Pauli channel and amplitude damping channel. Similarly, \mathcal{F} may also encompass noise channels like the amplitude damping channel, as well as the Pauli channel with equal probabilities for X and Y errors, e.g., depolarizing channel and dephasing channel.

These noise models are common physical processes that can occur in real quantum systems, hence the analysis can be applied to a wide range of practical scenarios. Therefore, only noise in ④ affects the behaviours of VCP significantly. The numerical simulations in Appendix C3 verify our analysis.

Furthermore, for multi-layer VCP, the analysis remains applicable for noise in ①, ② and ④. However, noise in ③ cannot be naturally ignored if it occurs in the middle of the circuit. It is important to note that the initial state of the ancillary subsystem for each VCP layer is reset to the maximally mixed state. Specifically, let the quantum state of the ancillary subsystem after noise in ③ be ρ . It holds that $\mathbb{E}_P(P\rho P) = I_{2^n}/2^n$, where P is the tensor product of single-qubit random Pauli unitaries [40]. Therefore, noise in ③ is automatically erased. Additionally, for the noise introduced by performing P , when the noise channel \mathcal{N} is unital, such as depolarizing and dephasing channels where $\mathcal{N}(I_d) = I_d$, they have no effect on VCP. Even for nonunital noise channels, such as the amplitude damping channel, since P is the tensor product of single-qubit random Pauli unitaries, with an error rate much lower than that of cSWAP gates, we can simplify the analysis by ignoring this noise.

In summary, for noise channel \mathcal{F} satisfying the condition defined in Theorem 1, only noise in ④ is critical to the performance of VCP. Therefore, PEC can be applied to mitigate noise in ④ for each VCP layer. If the noise channel \mathcal{F} violates the condition, PEC can also be applied to the control subsystem. Given that the control subsystem has a dimension of only 2, and PEC only needs to be applied to the number of locations proportional to the number of VCP layers, the cost of this part can be effectively managed. For simplicity, we primarily focus on the case where the condition holds. As a consequence, the additional cost of applying PEC involves characterizing the noise model, which can be accomplished using quantum process tomography [41, 42]. Although quantum process tomography generally requires exponential resources, in the context of our task, we only need to focus on the cSWAP gate. This targeted scenario significantly reduces the overhead, making the cost acceptable.

Figure 4(a) illustrates the enhanced framework for VCP, referred to as PVCP. In addition to the layer-wise implementation of VCP shown in Figures 2(c), the quantum gates G^i in the yellow boxes are performed on the target subsystem to mitigate errors via PEC. Please refer to Appendix B for more details on the optimal formation of G^i for several common types of noise channels. Additionally, the above conclusion also applies to VSP, as shown in Appendix C2. Therefore, the performance of VSP can also be enhanced using the circuit presented in Fig. 4(b), which is referred to as PVSP.

IV. ERROR ANALYSIS

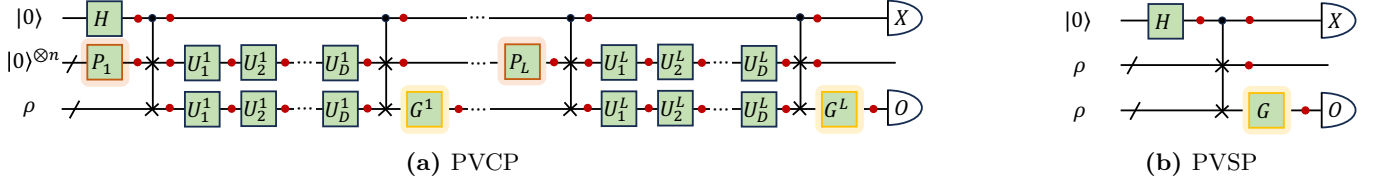


FIG. 4: Schemes of probabilistic virtual purification: (a) PVCP and (b) PVSP. Quantum gates G and G_i in the yellow boxes are random gates inserted to cancel the effect of noise in the target subsystem.

For different quantum metrology tasks, one common goal is to extract the information of unknown parameters λ from the expectation value $\text{tr}(O\rho)$, where ρ encodes λ and O is an observable. Let \hat{O} be a biased estimator of the noise-free expectation value $\langle O \rangle_\rho$, the corresponding mean squared error (MSE) is defined as

$$\text{MSE}(\hat{O}) = \mathbb{E} \left[\left(\hat{O} - \langle O \rangle_\rho \right)^2 \right] = \text{Bias}(\hat{O})^2 + \text{Var}(\hat{O})$$

with $\text{Bias}(\hat{O}) = \mathbb{E}[\hat{O}] - \langle O \rangle_\rho$ and $\text{Var}(\hat{O}) = \mathbb{E}[\hat{O}^2] - \mathbb{E}[\hat{O}]^2$.

Let $\rho = \mathcal{U}_D \circ \dots \circ \mathcal{U}_1(\rho_{\text{in}})$, their noisy implementation is represented by $\tilde{\rho} = \mathcal{E}_D \circ \mathcal{U}_D \circ \dots \circ \mathcal{E}_1 \circ \mathcal{U}_1(\rho_{\text{in}})$, where each noise channel \mathcal{E}_i is of an error rate p_i . Notice that $\mathcal{U} \circ \mathcal{E} = \mathcal{E}' \circ \mathcal{U}$, where $\mathcal{E}' = \mathcal{U} \circ \mathcal{E} \circ \mathcal{U}^\dagger$. Therefore, we can iteratively apply this relation to delay all noise channels at the end, i.e., $\tilde{\rho} = \mathcal{E}_{\text{tot}}(\rho)$. For simplicity, we assume the error components of \mathcal{E}_{tot} satisfy the orthogonality defined in Theorem 1, and the noise-free probability is approximated as $p_{\text{ideal}} = \prod_i (1 - p_i)$.

In single-layer m th-order PVCP, for noise channels satisfying Theorem 1 the noise increasing the systematic error only exists between the cSWAP layers, which can be merged into the noise channel \mathcal{E}_{tot} . Hence, the noise-free probability is increased from p_{ideal} to $p_{\text{ideal}}^{\text{VCP}-m} = p_{\text{ideal}}^m \hat{P}_m^{-1}$. Then, we have

$$\begin{aligned} |\text{Bias}(\hat{O})| &= |\text{tr}(O(\tilde{\rho} - \rho))| \\ &\leq \|O\|_\infty \|\tilde{\rho} - \rho\|_1 \\ &= (1 - p_{\text{ideal}}^{\text{VCP}-m}) \|O\|_\infty \|\hat{\rho} - \rho\|_1 \\ &\leq 2(1 - p_{\text{ideal}}^{\text{VCP}-m}) \|O\|_\infty \end{aligned}$$

where $\hat{\rho}$ is defined by $\tilde{\rho} = p_{\text{ideal}}^{\text{VCP}-m} \rho + (1 - p_{\text{ideal}}^{\text{VCP}-m}) \hat{\rho}$.

Furthermore, recall that PVCP constructs the estimator by division, specifically $\frac{\sum_i \alpha_i \langle X_i \rangle_{\tilde{\rho}_0}}{\sum_i \alpha_i \langle Y_i \rangle_{\tilde{\rho}_0}}$. Here, the observables $X \otimes O$ and $X \otimes I_{2^n}$ are modified to X_i and Y_i , respectively. These modified observables are performed on a same quantum state $\tilde{\rho}_0$, ensuring that $\langle X_i \rangle_{\tilde{\rho}_0} = \langle X \otimes O \rangle_{\tilde{\rho}_i}$ and $\langle Y_i \rangle_{\tilde{\rho}_0} = \langle X \otimes I_{2^n} \rangle_{\tilde{\rho}_i}$, where $\tilde{\rho}_i$ denotes the output state of the i -th PVCP circuit. The variance of this estimator can be approximated by

$$\text{Var} \left(\frac{x}{y} \right) \approx \frac{\mu_x^2}{\mu_y^2} \left(\frac{\text{Var}(x)}{\mu_x^2} - 2 \frac{\text{Cov}(x, y)}{\mu_x \mu_y} + \frac{\text{Var}(y)}{\mu_y^2} \right), \quad (1)$$

where x and y stands for the estimators of $\sum_i \alpha_i \langle X_i \rangle_{\tilde{\rho}_0}$ and $\sum_i \alpha_i \langle Y_i \rangle_{\tilde{\rho}_0}$, respectively, with expectation values

$\mu_x = \eta_m \text{tr}(O \hat{\mathcal{E}}^{(m)}(\rho))$ and $\mu_y = \eta_m$. Particularly, notice that observables $X \otimes O$ and $X \otimes I_{2^n}$ commute with each other, so they can be measured simultaneously in each circuit run. Hence, we assume that both the nominator and the denominator are estimated using ν circuit runs. By calculating the corresponding variances and covariance in Eq. (1), it can be derived that the sampling cost required to limit the variation to be ϵ^2 for a bounded observable O is $\nu = O \left(\frac{\gamma^2}{\epsilon^2 \eta_m^2} \right)$, where γ is value related to PEC that grows exponentially with the number n of qubits of ρ . Particularly, in the sequential scheme of quantum metrology, n is often kept constant. For more details, please refer to Appendix D.

In quantum metrology, the standard quantum limit (SQL) describes the error scaling with the number N of utilized encoding channels that is proportional to $1/N$. A faster decrease in MSE with N presents a quantum advantage. To observe the scaling of $\text{Bias}(\hat{O})^2$ and $\text{Var}(\hat{O})$ in N , a local single-parameter estimation task is considered. Assume that the estimator $\hat{\lambda}$ of λ is proportional to \hat{O}/N [23, 24]. Let $n = 1$, and suppose that the error rates for single-qubit gates and cSWAP gates are 0.001 and 0.05, respectively. Fig. 5(a) shows the corresponding results, with the black dashed line representing the noisy scenario without QEM for comparison. When N is less than 10^3 , PVCP notably reduces the bias. For $m = 2, 3$, the variance scaling continues to demonstrate a quantum advantage compared to the SQL, indicated by the grey dashed line. However, since $(1 - p)^N \approx pN$ for small p , when N exceeds 10^3 , the noise-free probability p_{ideal} can no longer dominate the noise channel \mathcal{E}_{tot} . Therefore, the advantage of single-layer PVCP in bias gradually vanishes, and the corresponding variance reaches its maximum value.

To further enhance the performance of PVCP, a multi-layer implementation can be employed. The scaling of bias and variance can be determined by extending the previous analysis. Fig. 5(b) presents the results for the 2nd-order PVCP. For small N , the single-layer implementation is most effective, as additional layers are impeded by noise introduced by the cSWAP gates. However, when N exceeds 100, the multi-layer PVCP outperforms the single-layer one, enabling higher precision in parameter estimation. For larger L , the value of N at which the bias of PVCP converges to the noisy case increases, demonstrating the effectiveness of the multi-layer PVCP. Additionally, although the variance (specifically, the value of

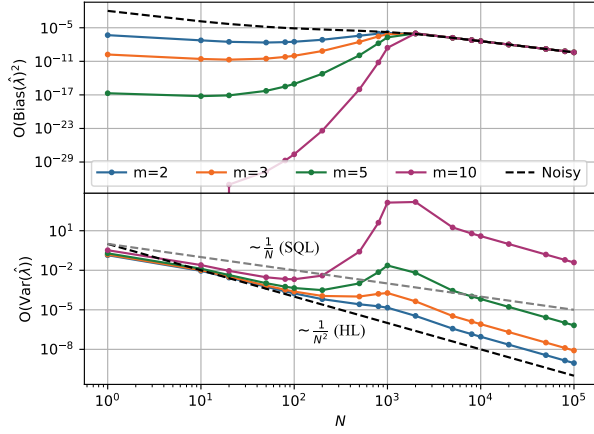
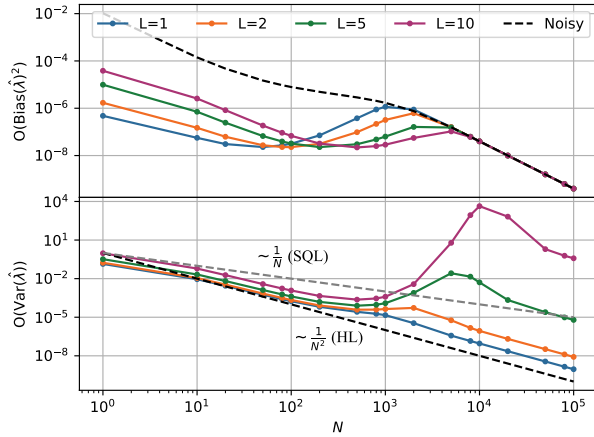
(a) Single-layer PVCP with different m (b) Multi-layer PVCP with $m = 2$

FIG. 5: Scaling of the bias and variance of $\hat{\lambda}$ under (a) various values of m with single-layer PVCP, and (b) various numbers of PVCP layers with $m = 2$.

γ) scales exponentially with the number of layers L , for probe states of constant size, the increase in variance can still be manageable under practical values of L .

Additionally, the analysis of variance in the Appendix D quantifies the statistical error introduced by each noise in the control subsystem. As discussed in Appendix E, the optimal cost to mitigate the noise can be higher than simply ignoring the noise. This finding is reasonable, as the sampling cost for QEM mentioned earlier is designed to handle arbitrary circuits, whereas the sampling cost we derived applies specifically to virtual purification-based quantum circuits. Nonetheless, this observation further underscores the efficiency of our protocol.

V. NUMERICAL SIMULATION

In this section, the performance and robustness of probabilistic virtual purification methods are evaluated for multi-parameter estimation tasks under various types of noise. In each scenario, we compare the behavior of five methods: the original noisy method, VSP, VCP, PVSP, and PVCP. Appendix F also presents the comparisons of these methods for single-parameter estimation tasks. Our observations indicate that the probabilistic virtual purification methods not only significantly improve the precision and sensitivity of quantum metrology, but also showcase the robustness against practical noises.

Specifically, we consider the Hamiltonian for a spin-1/2 in a magnetic field. The Hamiltonian is written as $H(\lambda) = B(\sin \theta \cos \phi X + \sin \theta \sin \phi Y + \cos \theta Z)$, where $\lambda = (B, \theta, \phi)$ are the unknown parameters to be estimated. Let the probe state be the maximally entangled state $|\psi\rangle = \frac{1}{\sqrt{2}}(|00\rangle + |11\rangle)$. The output state evolves under $U_\lambda = e^{-iH(\lambda)t} \otimes I_2$ for N times and is then measured using a Bell-state measurement. The Bell basis is defined as: $|\phi_1\rangle = |\psi\rangle$, $|\phi_2\rangle = \frac{1}{\sqrt{2}}(|00\rangle - |11\rangle)$, $|\phi_3\rangle = \frac{1}{\sqrt{2}}(|10\rangle + |01\rangle)$ and $|\phi_4\rangle = \frac{1}{\sqrt{2}}(|10\rangle - |01\rangle)$. In the noise-free case, the probabilities of obtaining each measurement outcome are

$$\begin{aligned} P(1|\lambda) &= \cos^2(BtN), \\ P(2|\lambda) &= \sin^2(BtN) \cos^2 \theta, \\ P(3|\lambda) &= \sin^2(BtN) \sin^2 \theta \cos^2 \phi, \\ P(4|\lambda) &= \sin^2(BtN) \sin^2 \theta \sin^2 \phi, \end{aligned} \quad (2)$$

which saturate the quantum Cramér-Rao bound [29].

A. Sequential scheme without feedback

Following the experimental setup mentioned above, we first evaluate the performance of different methods using the sequential scheme without feedback. Set $\lambda = (1, 0.9, 0.8)$ and $t = 0.001$. The error rates for single-qubit gates, two-qubit gates, and cSWAP gates are 0.001, 0.01, and 0.05, respectively. By obtaining the measurement outcome probability, the estimate $\hat{\lambda}$ can be derived from Eq. (2). Define the gap between $\hat{\lambda}$ and λ as $\|\lambda - \hat{\lambda}\|_1$. The performance of VCP and PVCP is presented at the optimal layer L^* , with a maximum of 3 layers.

For $N \in \{10, 50, 100, 200, 500, 800, 1,000\}$, Figs. 6(a)-(c) depict the performance of these methods under different noise conditions with infinite measurement shots. As observed, the probabilistic virtual purification methods significantly outperform other methods in the presence of depolarizing noise. PVSP performs well when N is small; however, as the error accumulates to a substantial level, it is surpassed by PVCP, which aligns with theoretical analysis. For dephasing and amplitude damping noise, PVCP shows superior performance with larger N ,

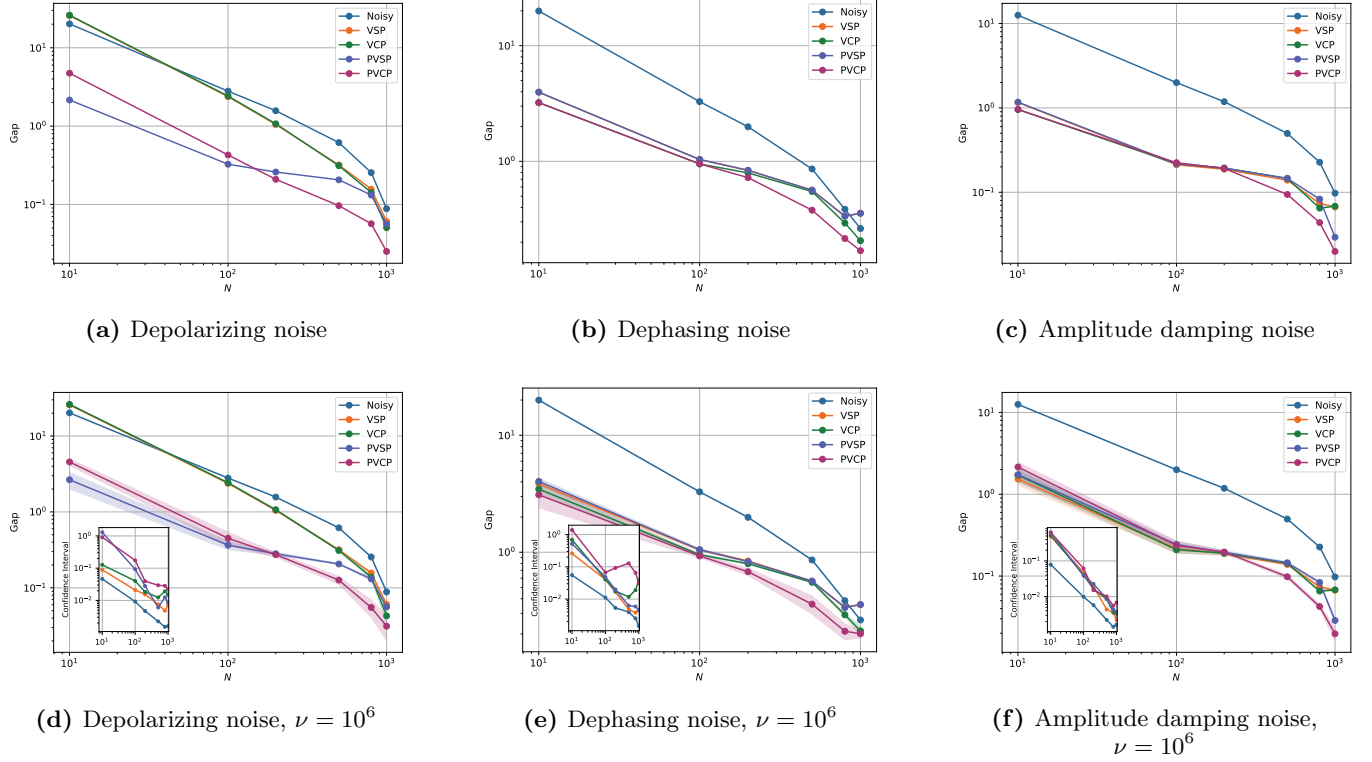


FIG. 6: Multi-parameter estimation gaps for different N under different types of noise channels. (a)-(c) plot the performance of different methods with infinite measurement shots, while (d)-(f) depict those with measurement shots $\nu = 10^6$. In scenarios with a limited number of measurement shots, experiments are conducted 10 times to calculate the mean values of the gaps and the 95% confidence intervals. These are represented by solid lines and shaded areas, respectively. Additionally, the exact values of these confidence intervals are provided in the inset subfigures.

highlighting its potential for application in complex circuits.

Furthermore, we also evaluate the behavior of these methods with a limited number of measurement shots, specifically $\nu = 10^6$. By repeating the experiments 10 times, Figs. 6(d)-(f) present the mean values of the gaps between the estimated and exact values for each method, depicted by solid lines. The shaded areas represent the corresponding 95% confidence intervals, with the exact values of these intervals detailed in the inset subfigure. Consistent with theoretical analysis, the error-mitigated estimators are more sensitive to variations in the sampled measurement outcomes, and all four QEM methods exhibit wider confidence intervals than the original noisy quantum circuits. However, the introduction of PEC does not significantly increase the confidence interval.

Additionally, in both the infinite and limited measurement shot number cases, the optimal number of layers for VCP is typically 1, whereas for PVCP, the optimal layers are often 2 or 3. By incorporating PEC, the errors introduced by the cSWAP gates are efficiently mitigated, allowing for more VCP layers, which further reduce the error in the target circuit.

B. Sequential feedback scheme

To further enhance the sensitivity of quantum metrology, the sequential feedback scheme is widely adopted. For the multi-parameter estimation task described above, the optimal control V_i after the i -th encoding unitary U_{λ} has been proved to be U_{λ}^{\dagger} for any i [29]. Therefore, for simplicity, we denote the optimal control as V without referencing i . Since λ is not known *a priori*, V can initially be set to the identity and then updated adaptively as $V = U_{\hat{\lambda}}^{\dagger}$, where $\hat{\lambda}$ is the estimated value of λ at each iteration. Instead of obtaining $\hat{\lambda}$ via Eq. (2), we now estimate λ using the maximum likelihood estimator [43]. Let $\mathbf{x} = (x_1, \dots, x_{\nu})$ with $x_i \in \{1, 2, 3, 4\}$ represents the sequence of measurement outcomes, and let the model (noise-free) distribution $Q_V(\mathbf{x}|\lambda)$ denote the probability of obtaining measurement outcomes \mathbf{x} given control V and parameters λ . Since $Q_V(\mathbf{x}|\lambda)$ can be calculated easily, an estimate $\hat{\lambda}$ can be obtained by minimizing the

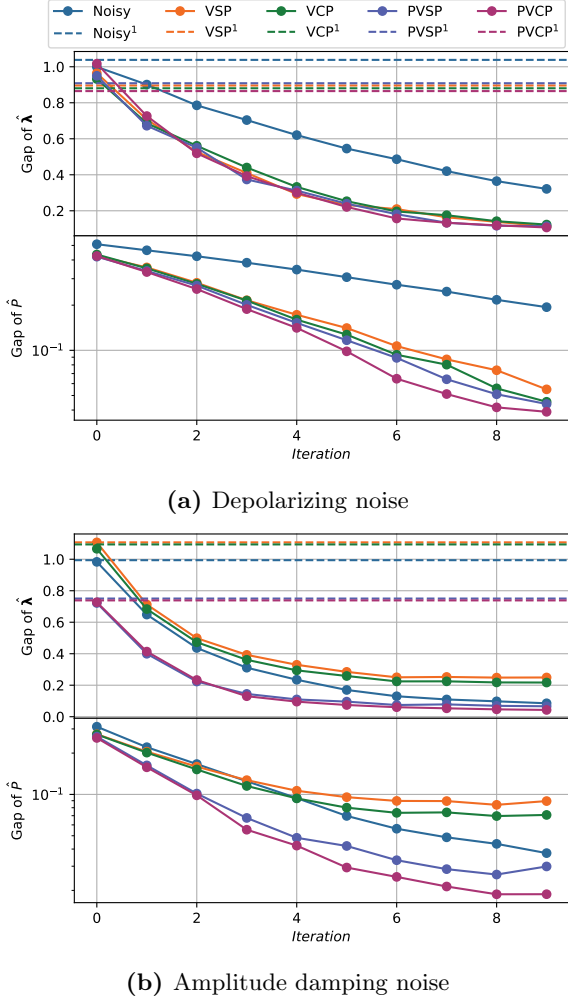


FIG. 7: Multi-parameter estimation gaps at different iterations under various types of noise channels. For each type of noise channel, the gaps of the estimated measurement outcome probability \hat{P}_V and the estimated parameters $\hat{\lambda}$ derived from \hat{P}_V at each iteration are plotted by solid lines. The number of measurement shots for each method is set to $\nu = 10^5$. For comparison, the corresponding estimations obtained from a single iteration optimization with measurement shots $\nu = 10^6$ are represented by dashed lines.

negative log-likelihood loss

$$\begin{aligned} & \arg \min_{\hat{\lambda}} -\log Q_V(\mathbf{x}|\hat{\lambda}) \\ &= \arg \min_{\hat{\lambda}} -\nu \sum_{x=1}^4 \hat{P}_V(x|\hat{\lambda}) \log Q_V(x|\hat{\lambda}), \end{aligned} \quad (3)$$

where \hat{P}_V refers to the empirical (noisy) distribution computed from \mathbf{x} . By repeatedly replacing V with $U_{\hat{\lambda}}^\dagger$ and optimizing Eq. (3) to find a new $\hat{\lambda}$, $\hat{\lambda}$ is expected to converge to λ .

To observe the behaviors of different methods, we set

$\lambda = (\frac{\pi}{4}, \frac{\pi}{6}, \frac{\pi}{6})$, and the output state is measured using a rotated Bell-state measurement by a local operation $e^{i\frac{\pi}{3\sqrt{3}}(X+Y+Z)}$. Additionally, let $N = 150$, $t = \frac{1}{2N}$, and suppose the error rates for single-qubit gates, two-qubit gates and cSWAP gates are 0.005, 0.01 and 0.025, respectively. For VCP and PVCP, the performance of the single-layer implementation is evaluated.

Set the number of iterations to 10, and each iteration with the measurement shots $\nu = 10^5$. By repeating the experiment 10 times, Fig. 7 depicts the average performance of different methods under different noise channels. Dephasing noise is not considered, as its effect does not vary much for different single-layer virtual purification-based circuits measuring on the computational basis. Specifically, the figure plots the gaps between the estimated measurement outcome probability \hat{P}_V and the noise-free probability P_V , i.e., $\|\hat{P}_V - P_V\|_1$, as well as the gaps between the estimated parameters $\hat{\lambda}$ derived from \hat{P}_V and the true parameters λ at each iteration for each type of noise channel, shown as solid lines. The results demonstrate that error-mitigated estimations significantly outperform the results of the original noisy quantum circuits for depolarizing noise. However, VSP and VCP do not achieve improved performance with QEM under amplitude damping noise, whereas both probabilistic virtual purification methods maintain their advantages. In particular, in these tasks PVCP achieves the highest precision for P_V , leading to the best estimation of λ .

As a comparison, the corresponding estimations from these methods obtained through a single iteration optimization with the same measurement cost, i.e., $\nu = 10^6$, are shown by dashed lines. The behavior of these methods generally remains consistent with previous observations, while highlighting the advantage of sequential feedback schemes over those without feedback control.

C. Robustness

In the previous analysis, the noise model was assumed to be local; however, in practice, the application of cSWAP gates can involve correlated noise. Furthermore, the implementation of probabilistic virtual purification methods requires the characterization of cSWAP gate noise. Due to the imperfections in quantum operations, accurately characterizing the noise model may be infeasible. To evaluate the robustness of our probabilistic virtual purification methods against practical noise, two types of noise models are considered for cSWAP gates: $\mathcal{E}_{\text{DP}}(p_0, p_1) = \circ_{i=1}^3 \mathcal{E}_{\text{DP}}^{(i)}(p_0) \circ \mathcal{E}_{\text{DP}}^{\text{global}}(p_1)$ and $\mathcal{E}_{\text{FP}}(p_0, p_1) = \circ_{i=1}^3 \mathcal{E}_{\text{PF}}^{(i)}(p_0) \circ \mathcal{E}_{\text{PF}}^{\text{global}}(p_1)$. Here, $\mathcal{E}_{\text{DP}}^{(i)}(p_0)$ ($\mathcal{E}_{\text{PF}}^{(i)}(p_0)$) refers to the local depolarizing (dephasing) channel with error rate p_0 acting on i -th qubit, while $\mathcal{E}_{\text{DP}}^{\text{global}}(p_1)$ ($\mathcal{E}_{\text{PF}}^{\text{global}}(p_1)$) represents the global depolarizing (global dephasing, i.e., $\mathcal{E}_{\text{PF}}^{\text{global}}(p_1) = (1-p)\mathcal{I}_{2^3} + p\mathcal{Z}^{\otimes 3}$) channel with error rate p_1 .

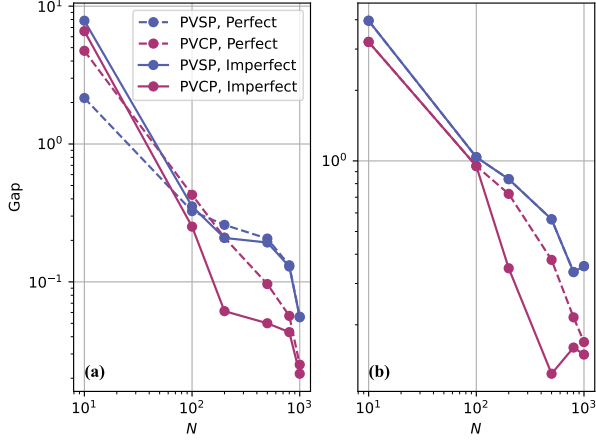


FIG. 8: Robustness of probabilistic virtual purification methods against cSWAP noise (a) $\mathcal{E}_{\text{DP}}(0.05, 0.01)$ and (b) $\mathcal{E}_{\text{PF}}(0.05, 0.01)$. For PVSP and PVCP, the PEC is designed to cancel local noise with a 10% relative error in the estimation of the error rate. Specifically, the PEC realizing the inverse of the corresponding local noise channel with an error rate of 0.055 is applied.

For each noise type, we assume a 10% relative error in estimating the error rate of cSWAP gates. Specifically, let the noise in cSWAP gates be $\mathcal{E}_{\text{DP}}(0.05, 0.01)$, and the PEC targeting canceling only the local noise $\circ_{i=1}^3 \mathcal{E}_{\text{DP}}^{(i)}(0.055)$ is applied. Analogously for $\mathcal{E}_{\text{PF}}(0.05, 0.01)$. Based on the experimental setup described in Sec. V A, Fig. 8 presents the corresponding results. The dashed lines display the results when PEC perfectly cancels cSWAP noise in the target subsystem, as shown in Figs. 6(a) and (b), while the solid lines represent the performance of these probabilistic virtual purification methods under practical noise with imperfect PEC cancellation of local noise. For PVSP, the gaps change little for depolarizing noise and remain unchanged for dephasing noise, as measurements are taken in the computational basis. Besides, PVCP achieves descent or even more precise parameter estimation for both types of noise. Thus, our probabilistic virtual purification methods demonstrate robustness against practical noise, indicating their potential for practical applications.

VI. CONCLUSION

Targeting significant noise accumulation and noisy implementations of QEM protocols, PVCP is proposed to achieve more precise estimations for unknown parameters on NISQ devices. Specifically, PVCP addresses the limitation of VSP in handling substantial noise accumulation, and fully exploits the efficacy of VCP. Moreover, it mitigates errors with a reasonable sampling cost, as the number of noise locations where PEC is applied is well managed. Additionally, our strategy for applying PEC can

be naturally adapted for VSP. For shallow circuits, PVSP can achieve comparable performance to PVCP, making it a good choice for practical applications due to its simpler implementation. The efficacy of these probabilistic virtual purification methods is systematically evaluated for both single- and multi-parameter estimation tasks under various types of noise channels, where a significant improvement is achieved compared with the original noisy and virtual purification methods. Notably, they also demonstrate robustness against correlated noise and the inexact characterization of noise models, underscoring their significance in practical applications.

Additionally, the scaling of bias and variance for PVCP has been analyzed. It was found that PVCP significantly reduces bias while maintaining a quantum advantage when the number of involved encoding unitaries is less than the inverse of the error rate of the encoding channel. This is consistent with numerical simulations for specific parameter estimation tasks. However, to further suppress noise beyond this range, the quantum advantage in variance scaling can disappear. Thus, incorporating a QEM method with QEC is necessary to achieve a practical quantum advantage [25]. We leave this integration for future work.

ACKNOWLEDGMENTS

We thank Ruiqi Zhang for helpful discussions. This work is supported by the Innovation Program for Quantum Science and Technology (2023ZD0300600), the Guangdong Provincial Quantum Science Strategic Initiative (GDZX2303007), the Research Grants Council of Hong Kong (14309223, 14309624, 14309022), 1+1+1 CUHK-CUHK(SZ)-GDST Joint Collaboration Fund (Grant No. GRDP2025-022).

Appendix A: Comparisons between virtual purification methods

To demonstrate and compare the efficacy of virtual state purification (VSP) and virtual channel purification (VCP) in mitigating systematic errors, we consider both the sequential scheme mentioned in the main text and the parallel scheme illustrated in Fig. 9. Specifically, a single-parameter estimation task is examined in the presence of three common types of local noise: depolarizing noise, dephasing noise, and amplitude damping noise.

Specifically, we consider a uniform magnetic field described by the Zeeman Hamiltonian $H = \sum_{j=1}^n \lambda Z^{(j)} / 2$ with unknown parameter λ determined by the targeting field, where $Z^{(j)}$ denotes the Pauli Z operator acting on the j -th qubit. In the parallel scheme, the initial probe state is selected as the n -qubit Greenberger-Horne-Zeilinger (GHZ) state, represented as $\rho_0 = |\text{GHZ}_n\rangle\langle\text{GHZ}_n|$, where $|\text{GHZ}_n\rangle = \frac{1}{\sqrt{2}}(|0\rangle^{\otimes n} + |1\rangle^{\otimes n})$. By measuring $P_y = |\text{GHZ}_y\rangle\langle\text{GHZ}_y|$, with

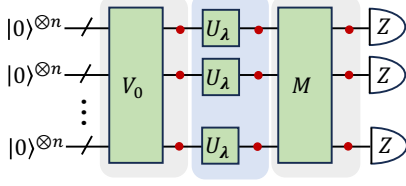


FIG. 9: Parallel scheme of quantum metrology. Green boxes represent quantum gates, while red circles indicate local noise occurring immediately after each quantum gate. Particularly, the first gray box, the blue box and the final gray box represent the state preparation stage, parameter encoding stage and measurement preparation stage, respectively. Subsequently, the output state is measured on a computational basis.

$|\text{GHZ}_y\rangle = \frac{1}{\sqrt{2}}(|0\rangle^{\otimes n} - i|1\rangle^{\otimes n})$, we derive $\lambda = \arcsin(1 - 2\langle P_y \rangle)/n$ [23]. Here, we set $n = N$. Similarly, in the sequential scheme, we use the same setting as the parallel scheme with $n = 1$, except that the Hamiltonian H is applied repeatedly N times.

With $N = 5$ and $m = 2$, VSP and single-layer VCP, referred to as VCP-1, are implemented using the quantum circuits depicted in Fig. 2(a) and (b), respectively. In these experiments, the error rates for single-qubit and two-qubit gates are set at 0.001 and $p \in [0.001, 0.02]$, respectively. Fig. 10 presents the resulting estimation errors, denoted as the gaps $|\lambda - \hat{\lambda}|$, obtained by applying VSP and VCP-1 without noise in the controlled-SWAP (cSWAP) gates (illustrated by the orange and green dashed lines, respectively). As the results indicate, both VSP and VCP significantly reduce errors compared to those obtained from the original noisy setup (represented by the blue solid line). Furthermore, VCP consistently demonstrates superior performance over VSP.

However, in practice, the cSWAP gate is notably noisy because its implementation requires at least five two-qubit gates [39]. Therefore, it is essential to evaluate the performance of these virtual purification methods under conditions where cSWAP gates are subject to noise. Specifically, the error rate for the cSWAP gates is set to $5p$, five times greater than that of two-qubit gates. As illustrated in Fig. 10, when noise is introduced into the cSWAP gates, the benefits of using VSP and VCP (depicted by the orange and green solid lines, respectively) are diminished or can even be negated in certain tasks. Thus, additional operations should be implemented to mitigate errors in cSWAP, thereby reducing errors in practical applications.

Appendix B: Probabilistic error cancellation

Probabilistic error cancellation (PEC) is a typical QEM protocol that inverts well-characterized noise channels, thereby canceling the effect of noise to obtain an un-

biased estimation of the noise-free expectation [19, 20]. Specifically, for an ideal quantum unitary channel \mathcal{U} , let $\{\mathcal{B}_i\}$ be a sufficiently large set of noisy quantum operations that can span it. This means we can decompose \mathcal{U} as $\mathcal{U} = \sum_i \alpha_i \mathcal{B}_i$, where α_i are real numbers satisfying $\sum_i \alpha_i = 1$. Then, for a target observable O on the quantum state $\mathcal{U}(\rho)$, it holds that

$$\langle O \rangle = \sum_i \alpha_i \text{tr}(O \mathcal{B}_i(\rho)) = \sum_i p_i \cdot \gamma \text{sign}(\alpha_i) \cdot \text{tr}(O \mathcal{B}_i(\rho)), \quad (\text{B1})$$

where $\gamma = \sum_i |\alpha_i| \geq 1$, $p_i = \frac{|\alpha_i|}{\gamma}$, and $\text{sign}(\cdot)$ indicates the sign of the real number. According to this equation, we can execute \mathcal{B}_i with probability p_i , and then multiply the corresponding measurement outcome by $\gamma \text{sign}(\alpha_i)$ to obtain an estimate. By repeating this procedure many times, the average value converges to the expectation value $\langle O \rangle$. To limit the variance to ϵ^2 , the number of trials required is $O(\gamma^2/\epsilon^2)$. More generally, to construct a sequence of ideal unitary channels $\mathcal{U} = \circ_{k=0}^{K-1} \mathcal{U}_k$, suppose each unitary channel can be decomposed into $\mathcal{U}_k = \sum_i \alpha_{k,i} \mathcal{B}_{k,i}$. Then, we have

$$\langle O \rangle = \sum_i \alpha_i \text{tr}(O \mathcal{B}_i(\rho)) = \sum_i p_i \cdot \gamma \text{sign}(\alpha_i) \cdot \text{tr}(O \mathcal{B}_i(\rho)),$$

where $\mathbf{i} = (i_0, i_1, \dots, i_{K-1})$, $\alpha_{\mathbf{i}} = \prod_{k=0}^{K-1} \alpha_{k,i_k}$, $\mathcal{B}_{\mathbf{i}} = \circ_{k=0}^{K-1} \mathcal{B}_{k,i_k}$, and $\gamma = \sum_{\mathbf{i}} |\alpha_{\mathbf{i}}| = \prod_k \gamma_k$ with $\gamma_k = \sum_{i_k} |\alpha_{k,i_k}|$. Hence, the sampling cost grows exponentially with K . The estimation of the expectation value follows the same procedure as in the single noise case.

According to the assumptions made in PEC [44], operators in the noisy basis $\{\mathcal{B}_i\}$ can be of the form $\mathcal{E} \circ \mathcal{G} \circ \mathcal{U}$, where \mathcal{G} is a quantum operation. For example, assume the local noise is the depolarizing channel \mathcal{E}_{DP} with error rate p . The optimal decomposition of the ideal unitary channel \mathcal{U} with respect to the minimal sampling cost is $\mathcal{U} = \sum_i \alpha_i \mathcal{E}_{DP} \circ \mathcal{G}_i \circ \mathcal{U}$, where α_i equal to $1 + \frac{3p}{4(1-p)}$ for $\mathcal{G}_0 = \mathcal{I}_2$ and equal to $-\frac{p}{4(1-p)}$ for $\mathcal{G}_{1,2,3} = \mathcal{X}, \mathcal{Y}, \mathcal{Z}$. Table I lists the corresponding coefficients α_i and noisy quantum operations \mathcal{B}_i that form the optimal decomposition of three common types of noise channels with respect to the minimal sampling cost.

Appendix C: Impact of noise in cSWAP gates

1. Proof of Theorem 1

First, we consider the 2nd-order VCP circuit. Suppose the channel of noisy operation is $\mathcal{U}_{\mathcal{E}} = \mathcal{E} \circ \mathcal{U}$, we then have

$$\begin{aligned} & \overline{\text{cSWAP}} \circ (\mathcal{I}_2 \otimes \mathcal{U}_{\mathcal{E}}^{\otimes 2}) \circ \overline{\text{cSWAP}} \\ &= \overline{\text{cSWAP}} \circ (\mathcal{I}_2 \otimes \mathcal{E}^{\otimes 2}) \circ \overline{\text{cSWAP}} \circ (\mathcal{I}_2 \otimes \mathcal{U}^{\otimes 2}), \end{aligned}$$

where $\overline{\text{cSWAP}}(\cdot) = \text{cSWAP}(\cdot)\text{cSWAP}^\dagger$ denotes the cSWAP channel. Therefore, we can examine the impact

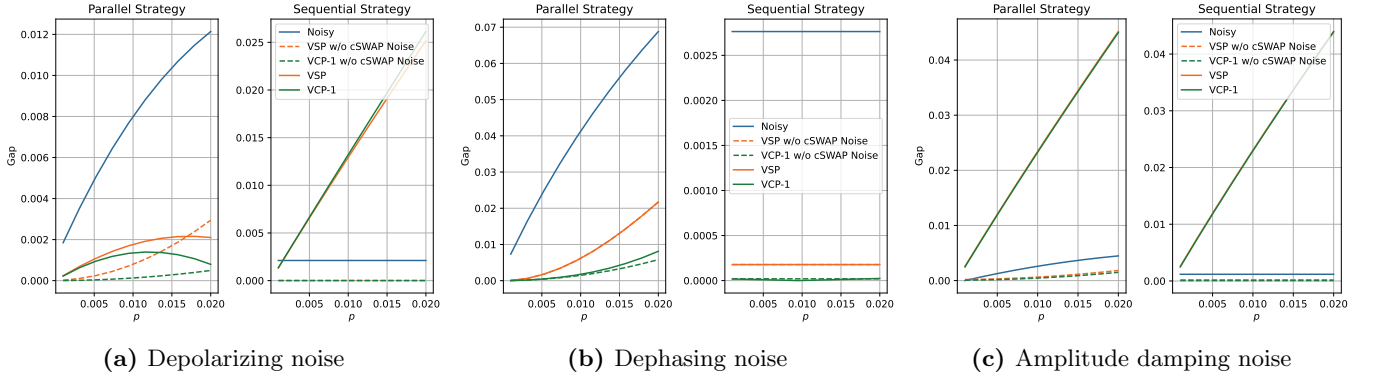


FIG. 10: Parameter estimation gaps under varying noise levels p for local (a) depolarizing noise, (b) dephasing noise, and (c) amplitude damping noise. The error rates for single-qubit and two-qubit gates are 0.001 and $p \in [0.001, 0.02]$. The gaps in the original quantum circuit, as well as those after applying VSP and VCP-1 under different p , are represented by the blue solid line, orange and green dashed lines, respectively. Besides, when noisy cSWAP gates are introduced, with an error rate of $5p$, the gaps following VSP and VCP-1 for different p are depicted by orange and green solid lines, respectively.

TABLE I: Optimal decompositions for different noise channels \mathcal{E} with noise level p [44]. For an ideal quantum unitary channel \mathcal{U} , it can be decomposed into $\mathcal{U} = \sum_i \alpha_i \mathcal{B}_i$. Quantum channels $\mathcal{X}, \mathcal{Y}, \mathcal{Z}$ stand for Pauli operators, and $\mathcal{P}_{|0\rangle}$ denotes the zero-state preparation channel.

	α	$\{\mathcal{B}_i\}$
Depolarizing	$\left(1 + \frac{3p}{4(1-p)}, -\frac{p}{4(1-p)}, -\frac{p}{4(1-p)}, -\frac{p}{4(1-p)}\right)$	$\{\mathcal{E} \circ \mathcal{U}, \mathcal{E} \circ \mathcal{X} \circ \mathcal{U}, \mathcal{E} \circ \mathcal{Y} \circ \mathcal{U}, \mathcal{E} \circ \mathcal{Z} \circ \mathcal{U}\}$
Dephasing	$\left(\frac{1-p}{1-2p}, -\frac{p}{1-2p}\right)$	$\{\mathcal{E} \circ \mathcal{U}, \mathcal{E} \circ \mathcal{Z} \circ \mathcal{U}\}$
Amplitude damping	$\left(\frac{1+\sqrt{1-p}}{2(1-p)}, \frac{1-\sqrt{1-p}}{2(1-p)}, -\frac{p}{1-p}\right)$	$\{\mathcal{E} \circ \mathcal{U}, \mathcal{E} \circ \mathcal{Z} \circ \mathcal{U}, \mathcal{E} \circ \mathcal{P}_{ 0\rangle}\}$

of noise in the control subsystem using the circuit depicted in Fig. 11 for simplicity.

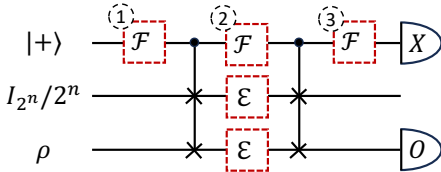


FIG. 11: Three locations where noise channel \mathcal{F} can occur in the control subsystem.

First, consider \mathcal{F} occurring only in the first two locations in Fig. 11. The state immediately before the second cSWAP gate is given by

$$\begin{aligned}
 \tilde{\rho} &= (\mathcal{F} \otimes \mathcal{E} \otimes \mathcal{E}) \circ \overline{\text{cSWAP}} \circ (\sigma \otimes I_{2^n} / 2^n \otimes \rho) \\
 &= 2^{-n} (\sigma_{00} \mathcal{F}(|0\rangle\langle 0|) \otimes \mathcal{E}^{\otimes 2}(I_{2^n} \otimes \rho) \\
 &\quad + \sigma_{01} \mathcal{F}(|0\rangle\langle 1|) \otimes \mathcal{E}^{\otimes 2}((I_{2^n} \otimes \rho) \text{SWAP}), \quad (\text{C1}) \\
 &\quad + \sigma_{10} \mathcal{F}(|1\rangle\langle 0|) \otimes \mathcal{E}^{\otimes 2}(\text{SWAP}(I_{2^n} \otimes \rho)) \\
 &\quad + \sigma_{11} \mathcal{F}(|1\rangle\langle 1|) \otimes \mathcal{E}^{\otimes 2}(\rho \otimes I_{2^n}))
 \end{aligned}$$

where $\sigma := \mathcal{F}(|+\rangle\langle +|)$ and σ_{ij} is the (i, j) -th entry of σ . The terms $\mathcal{F}(|0\rangle\langle 0|)$ and $\mathcal{F}(|1\rangle\langle 1|)$ can only expand

$\{|0\rangle\langle 0|, |1\rangle\langle 1|\}$. Since the cSWAP gate does not change their basis, their expectation values $\langle X \rangle$ of the control qubit measurement equal zero. Then, we can only focus on the middle two terms in Eq. (C1).

Define

$$\hat{\sigma} := \overline{\text{cSWAP}} (\mathcal{F}(|0\rangle\langle 1|) \otimes \mathcal{E}^{\otimes 2}((I_{2^n} / 2^n \otimes \rho) \text{SWAP})),$$

the corresponding measurement result is

$$\begin{aligned}
 \langle X \otimes O \rangle_{\hat{\sigma}} &= \sum_{i,j=0}^{4^n-1} \frac{p_i p_j}{2^n} \left[f_{01} \langle 1|X|0 \rangle \text{tr}(O E_i \rho E_j^\dagger) \text{tr}(E_j I_{2^n} E_i^\dagger) \right] \\
 &= f_{01} \sum_{i=0}^{4^n-1} p_i^2 e_i \text{tr}(O E_i \rho E_i^\dagger) \\
 &= f_{01} \cdot \hat{P}_2 \text{tr} \left(O \hat{\mathcal{E}}^{(2)} \rho \right)
 \end{aligned}$$

where $\hat{\mathcal{E}}^{(m)} = \hat{P}_m^{-1} \left(p_0^m e_0^{m-1} \mathcal{I} + \sum_{i=1}^{4^n-1} p_i^m e_i^{m-1} \overline{E_i} \right)$ with $\hat{P}_m = \sum_{i=0}^{4^n-1} p_i^m e_i^{m-1}$. Here, the second equality adopts the facts that $\text{tr}(E_i E_j^\dagger) = 0$ for all $i \neq j$ and $\text{tr}(E_i E_i^\dagger) / 2^n = e_i$. Similarly, for

$$\hat{\sigma}' := \overline{\text{cSWAP}} (\mathcal{F}(|1\rangle\langle 0|) \otimes \mathcal{E}^{\otimes 2}(\text{SWAP}(I_{2^n} / 2^n \otimes \rho))),$$

we have

$$\langle X \otimes O \rangle_{\hat{\sigma}'} = f_{10} \cdot \hat{P}_2 \text{tr} \left(O \hat{\mathcal{E}}^{(2)}(\rho) \right).$$

Consequently, for the state $\overline{\text{cSWAP}}(\tilde{\rho})$, we have

$$\begin{aligned} \langle X \otimes O \rangle_{\overline{\text{cSWAP}}(\tilde{\rho})} &= \sigma_{01} \langle X \otimes O \rangle_{\hat{\sigma}} + \sigma_{10} \langle X \otimes O \rangle_{\hat{\sigma}'} \\ &= (\sigma_{01} f_{01} + \sigma_{10} f_{10}) \cdot \hat{P}_2 \text{tr} \left(O \hat{\mathcal{E}}^{(2)}(\rho) \right), \\ &= \text{Real}(f_{01}^2) \hat{P}_2 \text{tr} \left(O \hat{\mathcal{E}}^{(2)}(\rho) \right) \end{aligned}$$

where $\text{Real}(\cdot)$ stands for the real part of the complex number. The last equality holds since $\sigma_{01} = \frac{1}{2} f_{01} = \sigma_{10}^*$, where $*$ denotes the conjugate.

Then, suppose \mathcal{F} also occurs in the last location, it can be easily checked that

$$\langle X \otimes O \rangle_{\tilde{\rho}_{\text{out}}} = \text{Real}(f_{01}^3) \hat{P}_2 \text{tr} \left(O \hat{\mathcal{E}}^{(2)}(\rho) \right) = \eta_2 \text{tr} \left(O \hat{\mathcal{E}}^{(2)}(\rho) \right), \quad (\text{C2})$$

here we define $\eta_m := \text{Real}(f_{01}^3) \hat{P}_m$. By setting $O = I_{2^n}$, the expectation value of the control qubit measurement is

$$\langle X \otimes I_{2^n} \rangle_{\tilde{\rho}_{\text{out}}} = \eta_2. \quad (\text{C3})$$

Furthermore, the above analysis can be easily generalized to the m th-order VCP, with $\langle X \otimes O \rangle_{\tilde{\rho}_{\text{out}}} = \eta_m \text{tr} \left(O \hat{\mathcal{E}}^{(m)}(\rho) \right)$ and $\langle X \otimes I_{2^n} \rangle_{\tilde{\rho}_{\text{out}}} = \eta_m$.

Notice that without the existence of \mathcal{F} , we have $\text{Real}(f_{01}^3) = 1$. In contrast, the noise in the control qubit usually results in $\text{Real}(f_{01}^3) < 1$. However, VCP obtains results by dividing Eq. (C2) by Eq. (C3), thus canceling the coefficient $\text{Real}(f_{01}^3)$, yielding the same value as the noise-free scenario.

2. Impact of noise in the control subsystem of the VSP circuit

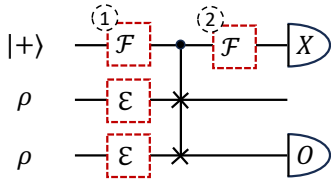


FIG. 12: Two locations where noise channel \mathcal{F} can occur in the control subsystem of the VSP circuit.

Lemma 1 Suppose noise channel $\mathcal{F} = \sum_{i=0}^3 q_i \overline{F_i}$ is a CPTP channel satisfies the properties

$$\mathcal{F}(|i\rangle\langle j|) = \begin{cases} f_{ij} |i\rangle\langle j|, & i \neq j \\ \sum_k f_k^{(i)} |k\rangle\langle k|, & i = j \end{cases}$$

where $f_{ij}, f_k^{(i)} \in \mathbb{C}$. Then, for a local noise channel \mathcal{F} and an n -qubit target quantum state ρ , it holds that

$$\frac{\langle X \otimes O \rangle_{\tilde{\rho}_{\text{out}}}}{\langle X \otimes I_{2^n} \rangle_{\tilde{\rho}_{\text{out}}}} = \frac{\langle X \otimes O \rangle_{\rho_{\text{out}}}}{\langle X \otimes I_{2^n} \rangle_{\rho_{\text{out}}}},$$

where $\tilde{\rho}_{\text{out}}$ and ρ_{out} denote the output states of the virtual state purification circuit, with and without the existence of \mathcal{F} , respectively.

Proof Starting with the 2nd-order VSP circuit, let $\tilde{\rho} = \mathcal{E}(\rho)$ and $\sigma := \mathcal{F}(|+\rangle\langle +|)$. The output state after the cSWAP gate is given by

$$\begin{aligned} \tilde{\rho}_{\text{out}} &= \overline{\text{cSWAP}} \circ (\sigma \otimes \tilde{\rho} \otimes \tilde{\rho}) \\ &= (\sigma_{00} \mathcal{F}(|0\rangle\langle 0|) + \sigma_{11} \mathcal{F}(|1\rangle\langle 1|)) \otimes \tilde{\rho}^{\otimes 2} \\ &\quad + \sigma_{01} f_{01} |0\rangle\langle 1| \otimes \tilde{\rho}^{\otimes 2} \text{SWAP} + \sigma_{10} f_{10} |1\rangle\langle 0| \otimes \text{SWAP} \tilde{\rho}^{\otimes 2}, \\ &= (\sigma_{00} \mathcal{F}(|0\rangle\langle 0|) + \sigma_{11} \mathcal{F}(|1\rangle\langle 1|)) \otimes \tilde{\rho}^{\otimes 2} \\ &\quad + (\sigma_{01} f_{01} |0\rangle\langle 1| + \sigma_{10} f_{10} |1\rangle\langle 0|) \otimes \sum_{ij} a_i a_j |ij\rangle\langle j i| \end{aligned}$$

where $\tilde{\rho} = \sum_i a_i |i\rangle\langle i|$ is the spectral decomposition of $\tilde{\rho}$. Then, we have

$$\begin{aligned} \langle X \otimes O \rangle_{\tilde{\rho}_{\text{out}}} &= (\sigma_{01} f_{01} + \sigma_{10} f_{10}) \sum_i a_i^2 \text{tr}(O |i\rangle\langle i|) \\ &= \text{Real}(f_{01}^2) \text{tr}(O \tilde{\rho}_{\text{out}}^2) \end{aligned}$$

since $\sigma_{01} = \frac{1}{2} f_{01} = \sigma_{10}^*$. Similarly, by setting $O = I_{2^n}$, it holds that $\langle X \otimes I \rangle_{\tilde{\rho}_{\text{out}}} = \text{Real}(f_{01}^2) \text{tr}(\tilde{\rho}_{\text{out}}^2)$. Analogously, for m th-order VSP, we have $\langle X \otimes O \rangle_{\tilde{\rho}_{\text{out}}} = \text{Real}(f_{01}^2) \text{tr}(O \tilde{\rho}_{\text{out}}^m)$ and $\langle X \otimes I \rangle_{\tilde{\rho}_{\text{out}}} = \text{Real}(f_{01}^2) \text{tr}(\tilde{\rho}_{\text{out}}^m)$. The coefficients introduced by \mathcal{F} can thus be canceled through division, resulting in the same value as in the noise-free scenario. This completes the proof.

3. Impact of noise in different locations of cSWAP gates

Following the numerical setup described in Appendix A, we now analyze the impact of various types of noise in the cSWAP gates within the single-layer VCP circuit numerically. The error rates for single-qubit, two-qubit, and cSWAP gates are assumed to be 0.001, 0.01, and 0.05, respectively. According to the categorization of noise types in the VCP circuit illustrated in Fig. 3, we consider three regions of noise affecting the cSWAP gates: ① noise in the control qubit of the cSWAP gates, ② noise in the last two subsystems between the two cSWAP layers, and ④ noise in the target subsystem after the second cSWAP layer of the VCP circuit. We ignore the noise in ③ as it does not affect the measurement expectation values. For each type of noise, we adjust the error rate from 0.05 to ten values evenly distributed from 0 to 0.05.

Set $N = 5$ and $m = 2$, Fig. 13 illustrates the corresponding numerical results, which align with the analysis

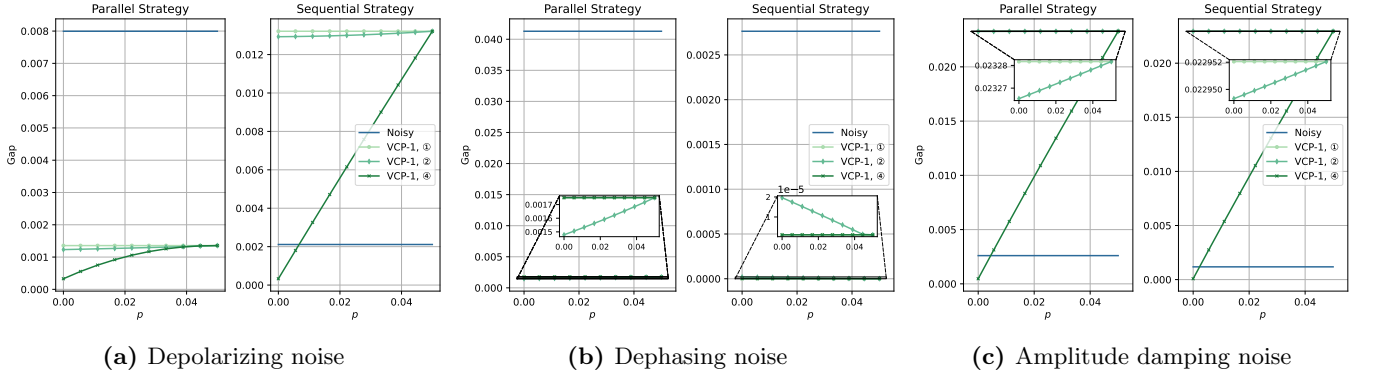


FIG. 13: Impacts of different types of noise in cSWAP gates for (a) depolarizing noise, (b) dephasing noise, and (c) amplitude damping noise. The light green, green, and dark green lines indicate the parameter estimation gaps after applying single-layer VCP under different error rates p for ① the control qubit of the cSWAP gate, ② the first cSWAP layer excluding the control qubit, and ④ the target subsystem of the second cSWAP layer, respectively. The blue line depicts the gaps in the original noisy quantum circuits.

above. First, the increasing error rate in ① does not affect the parameter estimation result, which introduces no systematic errors. Second, the gap under different error rates of noise in ② varies little, since it is suppressed automatically by VCP. As a comparison, noise in ④ enlarges the gap significantly with the increasing error rate. For depolarizing noise and amplitude damping noise, we can observe the benefits of VCP when the error rate in ④ is small. However, when the error rate becomes large, these advantages are diminished or may even lead to worse estimates, indicating the need for additional QEM methods to alleviate these effects. Dephasing noise is a special case since it does not affect the diagonal entries of the density matrix. As a result, the measurement outcome probabilities remain unchanged when measuring on a computational basis. Therefore, dephasing noise in ④ will not introduce errors in the estimates.

Appendix D: Variance of PVCP circuits

In the PVCP approach, the estimator is constructed by division as $\frac{\sum_i \alpha_i \langle X_i \rangle_{\tilde{\rho}_0}}{\sum_i \alpha_i \langle Y_i \rangle_{\tilde{\rho}_0}}$. In this formulation, the observables $X \otimes O$ and $X \otimes I_{2^n}$ are modified into X_i and Y_i , respectively, to allow their expectation values to be taken on the same quantum state $\tilde{\rho}_0$. This is done such that $\langle X_i \rangle_{\tilde{\rho}_0} = \langle X \otimes O \rangle_{\tilde{\rho}_i}$ and $\langle Y_i \rangle_{\tilde{\rho}_0} = \langle X \otimes I_{2^n} \rangle_{\tilde{\rho}_i}$, where $\tilde{\rho}_i$ is the output state of the i -th PVCP circuit. Suppose the nominator and the denominator are estimated using a number of ν circuit runs. Then, its variance can be calculated by

$$\text{Var} \left(\frac{x}{y} \right) \approx \frac{\mu_x^2}{\mu_y^2} \left(\frac{\text{Var}(x)}{\mu_x^2} - 2 \frac{\text{Cov}(x, y)}{\mu_x \mu_y} + \frac{\text{Var}(y)}{\mu_y^2} \right), \quad (\text{D1})$$

where x and y stands for the estimators of $\sum_i \alpha_i \langle X_i \rangle_{\tilde{\rho}_0}$ and $\sum_i \alpha_i \langle Y_i \rangle_{\tilde{\rho}_0}$, respectively, with expectation values $\mu_x = \eta_m \text{tr}(O \mathcal{E}^{(m)}(\rho))$ and $\mu_y = \eta_m$.

To calculate the variance of PVCP, we primarily focus on the scenario where the noise introduced by cSWAP gates satisfies the condition defined in Theorem 1. We start by considering the variance of VCP. The corresponding estimator is constructed as $\frac{\langle X \otimes O \rangle}{\langle X \otimes I_{2^n} \rangle}$, where the expectation values are taken from the output state of the VCP circuit. Let x' and y' be the estimators of $\langle X \otimes O \rangle$ and $\langle X \otimes I_{2^n} \rangle$, respectively. Follow the notations defined in Appendix C 1, and define the noise in both the ancillary and target subsystems introduced by cSWAP gates be \mathcal{F}' . Then, it can be easily derived that the expectation values of x' and y' are $\mu_{x'} = \eta_m \text{tr}(O \mathcal{F}' \circ \mathcal{E}^{(m)}(\rho))$ and $\mu_{y'} = \eta_m$, respectively.

Considering the case $m = 2$, for the variance of x' , we have

$$\text{Var}(x') = \frac{1}{\nu} (\langle I_2 \otimes O^2 \rangle - \langle X \otimes O \rangle^2).$$

To estimate $\langle I_2 \otimes O^2 \rangle$, the impact of the last noise in the control subsystem can be ignored since \mathcal{F} is trace-preserving. Then, it holds that

$$\begin{aligned} \langle I_2 \otimes O^2 \rangle &= \langle I_2 \otimes O^2 \rangle_{I_2 \otimes \mathcal{F}' \otimes \mathcal{F}' \left(\overline{\text{cSWAP}}_{(\tilde{\rho})} \right)} \\ &= \sigma_{00} f_0^{(0)} \langle 0 | I_2 | 0 \rangle \text{tr}(\mathcal{E}'(I_{2^n}/2^n)) \text{tr}(O^2 \mathcal{E}'(\rho)) \\ &\quad + \sigma_{00} f_1^{(0)} \langle 1 | I_2 | 1 \rangle \text{tr}(\mathcal{E}'(\rho)) \text{tr}(O^2 \mathcal{E}'(I_{2^n}/2^n)), \\ &\quad + \sigma_{11} f_0^{(1)} \langle 0 | I_2 | 0 \rangle \text{tr}(\mathcal{E}'(\rho)) \text{tr}(O^2 \mathcal{E}'(I_{2^n}/2^n)) \\ &\quad + \sigma_{11} f_1^{(1)} \langle 1 | I_2 | 1 \rangle \text{tr}(\mathcal{E}'(I_{2^n}/2^n)) \text{tr}(O^2 \mathcal{E}'(\rho)) \\ &= \alpha \text{tr}(O^2 \mathcal{E}'(\rho)) + \beta \text{tr}(O^2 \mathcal{E}'(I_{2^n}/2^n)) \end{aligned} \quad (\text{D2})$$

where $\tilde{\rho}$ is defined in Eq. (C1), $\mathcal{E}' = \mathcal{F}' \circ \mathcal{E}$, $\alpha = \sigma_{00} f_0^{(0)} +$

$\sigma_{11}f_1^{(1)}$ and $\beta = \sigma_{00}f_1^{(0)} + \sigma_{11}f_0^{(1)}$. Thus,

$$\text{Var}(x') = \frac{1}{\nu} \left\{ \alpha \text{tr}(O^2 \mathcal{E}'(\rho)) + \beta \text{tr}(O^2 \mathcal{E}'(I_{2^n}/2^n)) - \eta_2^2 \text{tr}(O \mathcal{F}' \circ \hat{\mathcal{E}}^{(2)}(\rho))^2 \right\} \quad (\text{D3})$$

Similarly, we have

$$\text{Var}(y') = \frac{1}{\nu} (\langle I_2 \otimes I_{2^n} \rangle - \langle X \otimes I_{2^n} \rangle^2) = \frac{1}{\nu} (1 - \eta_2^2) \quad (\text{D4})$$

Replacing O^2 with O in Eq. (D2), the covariance turns out to be

$$\begin{aligned} \text{Cov}(x', y') &= \frac{1}{\nu} \{ \langle I_2 \otimes O \rangle - \langle X \otimes O \rangle \langle X \otimes I_{2^n} \rangle \} \\ &= \frac{1}{\nu} \left\{ \alpha \text{tr}(O \mathcal{E}'(\rho)) + \beta \text{tr}(O \mathcal{E}'(I_{2^n}/2^n)) - \eta_2^2 \text{tr}(O \mathcal{F}' \circ \hat{\mathcal{E}}^{(2)}(\rho)) \right\} \quad (\text{D5}) \end{aligned}$$

Substituting Eqs. (D3), (D4) and (D5) into Eq. (D1), the final variance reads

$$\begin{aligned} &\text{Var}\left(\frac{x'}{y'}\right) \\ &\approx \frac{1}{\nu \eta_2^2} \left\{ \alpha \text{tr}(O^2 \mathcal{E}'(\rho)) + \beta \text{tr}(O^2 \mathcal{E}'(I_{2^n}/2^n)) - 2(\alpha \text{tr}(O \mathcal{E}'(\rho)) + \beta \text{tr}(O \mathcal{E}'(I_{2^n}/2^n))) \text{tr}(O \mathcal{F}' \circ \hat{\mathcal{E}}^{(2)}(\rho)) + \text{tr}(O \mathcal{F}' \circ \hat{\mathcal{E}}^{(2)}(\rho))^2 \right\} \\ &\leq \frac{1}{\nu \eta_2^2} \{ \|O^2\|_\infty + 3\|O\|_\infty^2 \} \quad (\text{D6}) \end{aligned}$$

where $\|\cdot\|_\infty$ denotes the spectral norm. Here, we assume η^2 is small since it exponentially decreases with the number of noise. The last inequality utilizes the fact that $\alpha, \beta \geq 0$ and $\alpha + \beta = 1$ since \mathcal{F} is a CPTP channel.

When considering PVCP, suppose the inverse noise operation \mathcal{F}'^{-1} is decomposed with coefficients α_i , where $\sum_i \alpha_i = 1$ and $\gamma = \sum_i |\alpha_i| \geq 1$. According to the analysis of PEC, it holds that $\text{Var}(x) = O(\gamma^2 \text{Var}(x'))$ [19, 20]. Besides, since PEC is applied only to the target subsystem and does not affect the measurement of the observable $X \otimes I_{2^n}$, we have $\text{Var}(y) = \text{Var}(y')$. For the covariance, it is given that $\text{Cov}(x, y) = \sum_{i,j} \alpha_i \alpha_j \text{Cov}(x_i, y_j)$, where x_i and y_j are the estimators for $\langle X_i \rangle_{\tilde{\rho}_0}$ and $\langle Y_j \rangle_{\tilde{\rho}_0}$, respectively. In line with the assumptions from Refs. [18, 45], we assume $\text{Cov}(x_i, y_j) \sim \text{Cov}(x', y')$ since the ensemble of circuits induced by PEC are variants of the primary circuit. Thus, the covariance can be simplified to $\text{Cov}(x, y) = \sum_{i,j} \alpha_i \alpha_j \text{Cov}(x', y') = \text{Cov}(x', y')$,

given that $\sum_i \alpha_i = 1$. As a consequence,

$$\begin{aligned} &\text{Var}\left(\frac{x}{y}\right) \\ &\approx \frac{\mu_x^2}{\mu_y^2} \left(\frac{\gamma^2 \text{Var}(x')}{\mu_x^2} - 2 \frac{\text{Cov}(x', y')}{\mu_x \mu_y} + \frac{\text{Var}(y')}{\mu_y^2} \right) \\ &\leq \frac{1}{\nu \eta_2^2} \left\{ \gamma^2 \|O^2\|_\infty + 3\|O\|_\infty^2 + \gamma^2 \eta_2^2 \text{tr}(O \mathcal{F}' \circ \hat{\mathcal{E}}^{(2)}(\rho))^2 + 2\eta_2^2 \text{tr}(O \mathcal{F}' \circ \hat{\mathcal{E}}^{(2)}(\rho)) \text{tr}(O \hat{\mathcal{E}}^{(2)}(\rho)) - \eta_2^2 \text{tr}(O \hat{\mathcal{E}}^{(2)}(\rho))^2 \right\} \\ &\leq \frac{1}{\nu \eta_2^2} \{ \gamma^2 \|O^2\|_\infty + (\gamma^2 \eta_2^2 + 2\eta_2^2 + 3)\|O\|_\infty^2 \} \quad (\text{D7}) \end{aligned}$$

Considering a bounded observable O , to limit the variation to be ϵ^2 , the sampling cost scales as $\nu = O\left(\frac{\gamma^2}{\epsilon^2 \eta_2^2}\right)$. For the case where $m \geq 2$, it can be verified that the sampling cost similarly scales as $\nu = O\left(\frac{\gamma^2}{\epsilon^2 \eta_m^2}\right)$. Additionally, since O is a bounded observable, a similar result can be obtained even without the assumption that $\text{Cov}(x_i, y_j) \sim \text{Cov}(x', y')$.

Appendix E: Comparative analysis of sampling costs for noise in the control subsystem of VCP circuits

The analysis of variance in the Appendix D indicates that the statistical error introduced by each noise in the control subsystem is characterized by $\text{Real}(f_{01})^{-2}$. It is interesting to compare the sampling cost amplified by the noise in the control qubit with the sampling cost of introducing other QEM protocols to mitigate this noise.

Case 1. Let \mathcal{F} be a dephasing channel, with noise level $p \in [0, 1]$, i.e.,

$$\mathcal{F}(\rho) = (1 - p)\rho + pZ\rho Z.$$

Then, we have $\text{Real}(f_{01}) = 1 - 2p$. Hence, the additional sampling cost introduced by each dephasing noise equals $(1 - 2p)^{-2}$, which matches the optimal cost for mitigating it [44, 46].

Case 2. Let \mathcal{F} be a depolarizing channel, with noise level $p \in [0, 1]$, that maps a quantum state ρ into

$$\mathcal{F}(\rho) = (1 - p)\rho + \frac{p}{2}I_2.$$

It can be easily found that $\text{Real}(f_{01}) = 1 - p$, which indicates that the additional sampling cost introduced by each depolarizing noise is $(1 - p)^{-2}$. As a comparison, it has been proved that the optimal cost to mitigate depolarizing noise requires $\left(\frac{1+p/2}{1-p}\right)^2$ [44, 46], which is clearly greater than simply ignoring the noise.

Case 3. Let \mathcal{F} be a amplitude damping channel, with Kraus operators $F_0 = |0\rangle\langle 0| + \sqrt{1-p}|1\rangle\langle 1|$ and $F_1 =$

$\sqrt{p}|0\rangle\langle 1|$, that maps a quantum state ρ into

$$\mathcal{F}(\rho) = F_0 \rho F_0^\dagger + F_1 \rho F_1^\dagger,$$

where $p \in [0, 1]$. Then, it holds that $\text{Real}(f_{01}) = \sqrt{1-p}$, indicating that the sampling cost is amplified by a factor of $(1-p)^{-1}$ for each instance of amplitude damping noise. In contrast, the minimal cost to mitigate the amplitude damping noise is shown to be $\left(\frac{1+p}{1-p}\right)^2$ [46]. Once again, it is more efficient to do nothing regarding this type of noise in the control subsystem.

These results are reasonable because the sampling cost for QEM we mentioned above is designed to handle arbitrary circuits, whereas the sampling cost $\text{Real}(f_{01})^{-2}$ applies specifically to virtual purification-based circuits. It can be easily verified that the comparisons in these cases also hold for VSP circuits. Nonetheless, the properties we have discovered are valuable for designing an efficient framework to enhance the efficacy of these virtual purification methods.

Appendix F: Numerical simulation: single-parameter estimation

In the context of the Zeeman Hamiltonian discussed in Appendix A, we evaluate the efficacy of five methods: noisy method, VSP, VCP, PVSP and PVCP. In specific, a sequential scheme is considered, where the Hamiltonian $H = \lambda Z/2$ is applied N times in sequence. Let the local parameter $\lambda = \frac{\pi}{4} \times 10^{-4}$, and $N \in \{10, 50, 100, 200, 500, 800, 1,000\}$. Suppose the error rates for single-qubit gates and cSWAP gates are 0.001 and 0.05, respectively. Particularly for VCP and PVCP, a layer-wise implementation is employed with a maximum of 5 layers, and the following results present their performance at the optimal layer L^* .

Figs. 14(a)-(c) illustrate the corresponding results with an infinite number of measurement shots. Without the assistance of PEC, the original virtual purification methods offer limited advantages over the performance of the original noisy circuit and may even exhibit worse behavior in some instances. However, the introduction of PEC significantly enhances the performance of both virtual

purification methods. This aligns with theoretical analysis, which suggests that PVSP performs well when the accumulated error is low (i.e., when N is small), whereas PVCP generally exhibits a clear advantage over PVSP across most scenarios. With an infinite number of measurement shots, the optimal layers L^* for VCP under different values of N are generally 1 or 2, while PVCP achieves optimal performance with 5 layers in most cases. Thus, by incorporating PEC, additional VCP layers can be utilized to further suppress errors.

In addition, we assess the behavior of these methods with a limited number of measurement shots, specifically $\nu = 10^7$. By repeating the experiments 10 times, Figs. 14(d)-(f) display the mean values of the gaps between the estimated and exact values for each method, illustrated by solid lines. The shaded areas represent the corresponding 95% confidence intervals, with the exact values of these intervals detailed in the inset subfigure. Similar to the multi-parameter estimation tasks represented in the main text, the error-mitigated estimators are more sensitive to variations in the sampled measurement outcomes, and all four QEM methods exhibit wider confidence intervals than the original noisy quantum circuits. For example, when $N = 1,000$, VCP and PVCP display wider confidence intervals compared to VSP and PVSP. However, the introduction of PEC does not significantly increase the confidence interval. Moreover, the range of gaps for PVCP is generally smaller than those of the other methods, underscoring its practical effectiveness. Furthermore, the optimal number of layers L^* for VCP typically remains 1 or 2, while for PVCP, it is usually reduced to 2 or 3 under a limited number of measurement shots, as additional VCP layers tend to increase variance.

In quantum metrology, it is generally expected that the gap between estimated and true values decreases as N increases. However, in this scenario, higher precision is achieved only when N is roughly less than 100. Beyond this point, the presence of noise diminishes the benefit of repeated use of the encoding channel \mathcal{U}_λ . Nevertheless, when λ approaches zero, which corresponds to a larger Fisher information, our additional numerical simulations indicate that the gap indeed decreases with increasing N . This observation also highlights the advantage of the sequential feedback scheme.

-
- [1] V. Giovannetti, S. Lloyd, and L. Maccone, Phys. Rev. Lett. **96**, 010401 (2006).
 - [2] V. Giovannetti, S. Lloyd, and L. Maccone, Nature Photonics **5**, 222 (2011).
 - [3] C. L. Degen, F. Reinhard, and P. Cappellaro, Rev. Mod. Phys. **89**, 035002 (2017).
 - [4] L. Pezzè, A. Smerzi, M. K. Oberthaler, R. Schmied, and P. Treutlein, Rev. Mod. Phys. **90**, 035005 (2018).
 - [5] B. M. Escher, R. L. de Matos Filho, and L. Davidovich, Nature Physics **7**, 406 (2011).
 - [6] R. Demkowicz-Dobrzański, J. Kołodyński, and M. Guţă, Nature Communications **3**, 1063 (2012).
 - [7] J. F. Haase, A. Smirne, S. F. Huelga, J. Kołodyński, and R. Demkowicz-Dobrzański, Quantum Measurements and Quantum Metrology **5**, 13 (2016).
 - [8] E. M. Kessler, I. Lovchinsky, A. O. Sushkov, and M. D. Lukin, Phys. Rev. Lett. **112**, 150802 (2014).
 - [9] W. Dür, M. Skotiniotis, F. Fröwis, and B. Kraus, Phys. Rev. Lett. **112**, 080801 (2014).
 - [10] X.-M. Lu, S. Yu, and C. H. Oh, Nature Communications

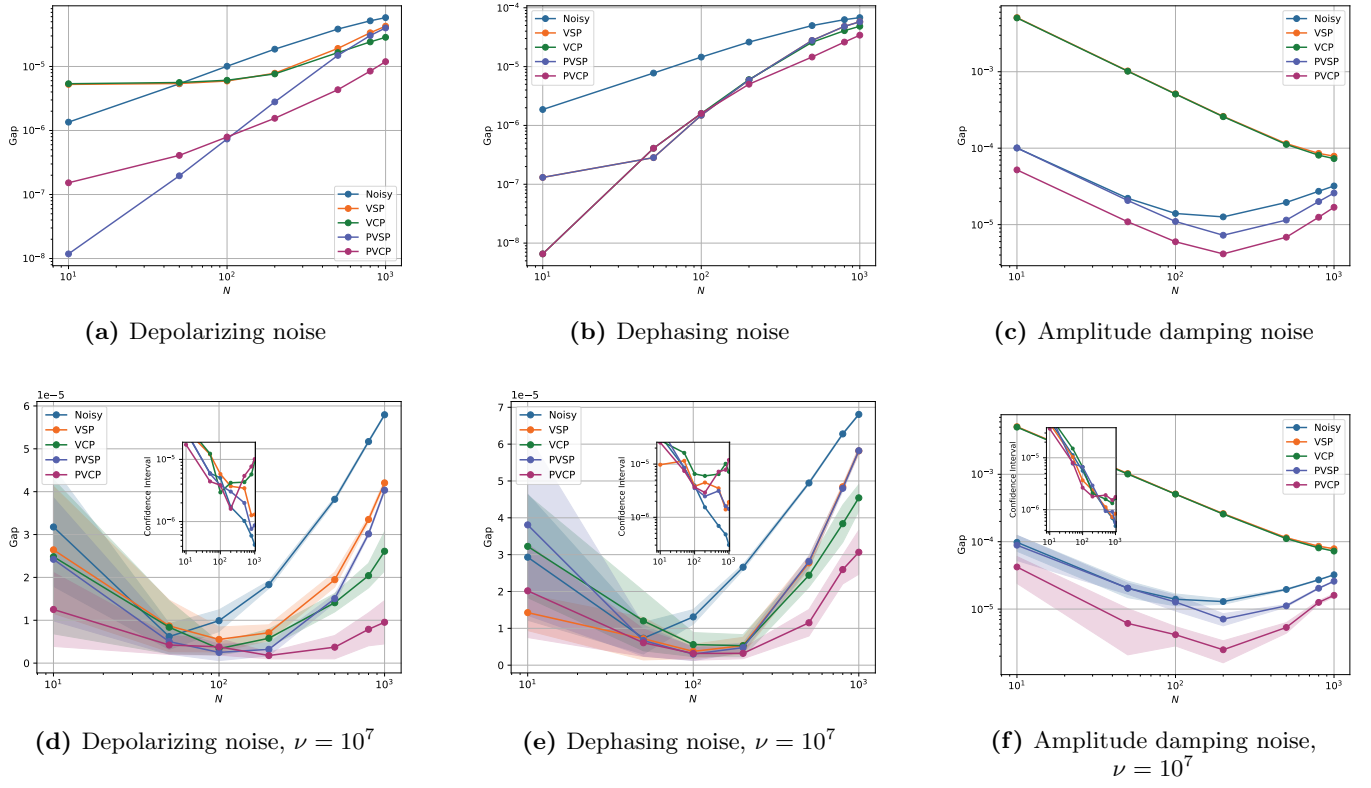


FIG. 14: Single-parameter estimation gaps for different N under different types of noise channels. (a)-(c) plot the performance of different methods with infinite measurement shots, while (d)-(f) depict those with measurement shots $\nu = 10^7$. In scenarios with a limited number of measurement shots, experiments are conducted 10 times to calculate the mean values of the gaps and the 95% confidence intervals. These are represented by solid lines and shaded areas, respectively. Additionally, the exact values of these confidence intervals are provided in the inset subfigures.

- 6, 7282 (2015).
- [11] D. A. Herrera-Martí, T. Gefen, D. Aharonov, N. Katz, and A. Retzker, *Phys. Rev. Lett.* **115**, 200501 (2015).
 - [12] D. Layden, S. Zhou, P. Cappellaro, and L. Jiang, *Phys. Rev. Lett.* **122**, 040502 (2019).
 - [13] S. Zhou, M. Zhang, J. Preskill, and L. Jiang, *Nature Communications* **9**, 78 (2018).
 - [14] R. Acharya, D. A. Abanin, L. Aghababaie-Beni, I. Aleiner, T. I. Andersen, M. Ansmann, F. Arute, K. Arya, A. Asfaw, N. Astrakhantsev, J. Atalaya, R. Babbush, D. Bacon, B. Ballard, J. C. Bardin, J. Bausch, A. Bengtsson, A. Bilmes, S. Blackwell, S. Boixo, G. Bortoli, A. Bourassa, J. Bovaird, L. Brill, M. Broughton, D. A. Browne, B. Buchea, B. B. Buckley, D. A. Buell, T. Burger, B. Burkett, N. Bushnell, A. Cabrera, J. Campero, H.-S. Chang, Y. Chen, Z. Chen, B. Chiaro, D. Chik, C. Chou, J. Claes, A. Y. Cleland, J. Cogan, R. Collins, P. Conner, W. Courtney, A. L. Crook, B. Curtin, S. Das, A. Davies, L. De Lorenzo, D. M. Debroy, S. Demura, M. Devoret, A. Di Paolo, P. Donohoe, I. Drozdov, A. Dunsworth, C. Earle, T. Edlich, A. Eickbusch, A. M. Elbag, M. Elzouka, C. Erickson, L. Faoro, E. Farhi, V. S. Ferreira, L. F. Burgos, E. Forati, A. G. Fowler, B. Foxen, S. Ganjam, G. Garcia, R. Gasca, É. Genois, W. Jiang, C. Gidney, D. Gilboa, R. Gosula, A. G. Dau, D. Graumann, A. Greene, J. A. Gross, S. Habegger, J. Hall, M. C. Hamilton, M. Hansen, M. P. Harrigan, S. D. Harrington, F. J. H. Heras, S. Heslin, P. Heu, O. Higgott, G. Hill, J. Hilton, G. Holland, S. Hong, H.-Y. Huang, A. Huff, W. J. Huggins, L. B. Ioffe, S. V. Isakov, J. Iveland, E. Jeffrey, Z. Jiang, C. Jones, S. Jordan, C. Joshi, P. Juhas, D. Kafri, H. Kang, A. H. Karamlou, K. Kechedzhi, J. Kelly, T. Khairé, T. Khattar, M. Khezri, S. Kim, P. V. Klimov, A. R. Klots, B. Kobrin, P. Kohli, A. N. Korotkov, F. Kostritsa, R. Kothari, B. Kozlovskii, J. M. Kreikebaum, V. D. Kurilovich, N. Lacroix, D. Landhuis, T. Lange-Dei, B. W. Langley, P. Laptev, K.-M. Lau, L. Le Guevel, J. Ledford, J. Lee, K. Lee, Y. D. Lensky, S. Leon, B. J. Lester, W. Y. Li, Y. Li, A. T. Lill, W. Liu, W. P. Livingston, A. Locharla, E. Lucero, D. Lundahl, A. Lunt, S. Madhuk, F. D. Malone, A. Maloney, S. Mandrà, J. Manyika, L. S. Martin, O. Martin, S. Martin, C. Maxfield, J. R. McClean, M. McEwen, S. Meeks, A. Megrant, X. Mi, K. C. Miao, A. Mieszala, R. Molavi, S. Molina, S. Montazeri, A. Morvan, R. Movassagh, W. Mruczkiewicz, O. Naaman, M. Neeley, C. Neill, A. Nersisyan, H. Neven, M. Newman, J. H. Ng, A. Nguyen, M. Nguyen, C.-H. Ni, M. Y. Niu, T. E. O'Brien, W. D. Oliver, A. Opremcak, K. Ottosson, A. Petukhov, A. Pizzuto, J. Platt, R. Potter, O. Pritchard, L. P. Pryadko, C. Quintana, G. Ramachandran, M. J. Reagor, J. Redding, D. M. Rhodes, G. Roberts, E. Rosenberg, E. Rosenfeld, P. Roushan,

- N. C. Rubin, N. Saei, D. Sank, K. Sankaragomathi, K. J. Satzinger, H. F. Schurkus, C. Schuster, A. W. Senior, M. J. Shearn, A. Shorter, N. Shutty, V. Shvarts, S. Singh, V. Sivak, J. Skruzny, S. Small, V. Smelyanskiy, W. C. Smith, R. D. Somma, S. Springer, G. Sterling, D. Strain, J. Suchard, A. Szasz, A. Szein, D. Thor, A. Torres, M. M. Torunbalci, A. Vaishnav, J. Vargas, S. Vdovichev, G. Vidal, B. Villalonga, C. V. Heidweiller, S. Waltman, S. X. Wang, B. Ware, K. Weber, T. Weidel, T. White, K. Wong, B. W. K. Woo, C. Xing, Z. J. Yao, P. Yeh, B. Ying, J. Yoo, N. Yosri, G. Young, A. Zalcman, Y. Zhang, N. Zhu, N. Zobrist, G. Q. AI, and Collaborators, *Nature* **638**, 920 (2025).
- [15] Y. Zhao, Y. Ye, H.-L. Huang, Y. Zhang, D. Wu, H. Guan, Q. Zhu, Z. Wei, T. He, S. Cao, F. Chen, T.-H. Chung, H. Deng, D. Fan, M. Gong, C. Guo, S. Guo, L. Han, N. Li, S. Li, Y. Li, F. Liang, J. Lin, H. Qian, H. Rong, H. Su, L. Sun, S. Wang, Y. Wu, Y. Xu, C. Ying, J. Yu, C. Zha, K. Zhang, Y.-H. Huo, C.-Y. Lu, C.-Z. Peng, X. Zhu, and J.-W. Pan, *Phys. Rev. Lett.* **129**, 030501 (2022).
- [16] Z. Ni, S. Li, X. Deng, Y. Cai, L. Zhang, W. Wang, Z.-B. Yang, H. Yu, F. Yan, S. Liu, C.-L. Zou, L. Sun, S.-B. Zheng, Y. Xu, and D. Yu, *Nature* **616**, 56 (2023).
- [17] Z. Zimborás, B. Koczor, Z. Holmes, E.-M. Borrelli, A. Gilyén, H.-Y. Huang, Z. Cai, A. Acín, L. Aolita, L. Banchi, *et al.*, arXiv preprint arXiv:2501.05694 (2025).
- [18] Z. Cai, R. Babbush, S. C. Benjamin, S. Endo, W. J. Huggins, Y. Li, J. R. McClean, and T. E. O’Brien, *Rev. Mod. Phys.* **95**, 045005 (2023).
- [19] K. Temme, S. Bravyi, and J. M. Gambetta, *Phys. Rev. Lett.* **119**, 180509 (2017).
- [20] S. Endo, S. C. Benjamin, and Y. Li, *Phys. Rev. X* **8**, 031027 (2018).
- [21] A. Lowe, M. H. Gordon, P. Czarnik, A. Arrasmith, P. J. Coles, and L. Cincio, *Phys. Rev. Res.* **3**, 033098 (2021).
- [22] W. J. Huggins, S. McArdle, T. E. O’Brien, J. Lee, N. C. Rubin, S. Boixo, K. B. Whaley, R. Babbush, and J. R. McClean, *Phys. Rev. X* **11**, 041036 (2021).
- [23] K. Yamamoto, S. Endo, H. Hakoshima, Y. Matsuzaki, and Y. Tokunaga, *Phys. Rev. Lett.* **129**, 250503 (2022).
- [24] H. Kwon, C. Oh, Y. Lim, H. Jeong, and L. Jiang, *Phys. Rev. A* **109**, 022410 (2024).
- [25] H. Kwon, C. Oh, Y. Lim, H. Jeong, S.-W. Lee, and L. Jiang, “Virtual purification complements quantum error correction in quantum metrology,” (2025), arXiv:2503.12614 [quant-ph].
- [26] Y. Hama and H. Nishi, arXiv preprint arXiv:2303.01820 (2023).
- [27] B. Koczor, *Phys. Rev. X* **11**, 031057 (2021).
- [28] Z. Liu, X. Zhang, Y.-Y. Fei, and Z. Cai, “Virtual channel purification,” arXiv:2402.07866 [quant-ph] (2024).
- [29] H. Yuan, *Phys. Rev. Lett.* **117**, 160801 (2016).
- [30] K. Tsubouchi, T. Sagawa, and N. Yoshioka, *Phys. Rev. Lett.* **131**, 210601 (2023).
- [31] R. Takagi, H. Tajima, and M. Gu, *Phys. Rev. Lett.* **131**, 210602 (2023).
- [32] R. Takagi, S. Endo, S. Minagawa, and M. Gu, *npj Quantum Information* **8**, 114 (2022).
- [33] G. Chiribella, G. M. D’Ariano, P. Perinotti, and B. Valiron, *Phys. Rev. A* **88**, 022318 (2013).
- [34] X. Zhao, Y. Yang, and G. Chiribella, *Phys. Rev. Lett.* **124**, 190503 (2020).
- [35] M. T. Quintino, Q. Dong, A. Shimbo, A. Soeda, and M. Murao, *Phys. Rev. Lett.* **123**, 210502 (2019).
- [36] J. Bavaresco, M. Murao, and M. T. Quintino, *Phys. Rev. Lett.* **127**, 200504 (2021).
- [37] Z. Cai and S. C. Benjamin, *Scientific Reports* **9**, 11281 (2019).
- [38] J. J. Wallman and J. Emerson, *Phys. Rev. A* **94**, 052325 (2016).
- [39] J. A. Smolin and D. P. DiVincenzo, *Phys. Rev. A* **53**, 2855 (1996).
- [40] A. Roy and A. J. Scott, *Designs, codes and cryptography* **53**, 13 (2009).
- [41] I. L. Chuang and M. A. Nielsen, *Journal of Modern Optics* **44**, 2455 (1997).
- [42] S. T. Merkel, J. M. Gambetta, J. A. Smolin, S. Poletto, A. D. Córcoles, B. R. Johnson, C. A. Ryan, and M. Steffen, *Phys. Rev. A* **87**, 062119 (2013).
- [43] R. A. Fisher, *Philosophical Transactions of the Royal Society of London. Series A, Containing Papers of a Mathematical or Physical Character* **222**, 309 (1922).
- [44] R. Takagi, *Phys. Rev. Res.* **3**, 033178 (2021).
- [45] Z. Cai, “A practical framework for quantum error mitigation,” (2023), arXiv:2110.05389 [quant-ph].
- [46] J. Jiang, K. Wang, and X. Wang, *Quantum* **5**, 600 (2021).